MODEL CATALYSTS FOR HIGH-PRESSURE

SPECTROSCOPIC INVESTIGATIONS

by

John Elliott Bedenbaugh

A thesis submitted to the Faculty of the University of Delaware in partial
fulfillment of the requirements for the degree of Master of Chemical Engineering

Fall 2009

MODEL CATALYSTS FOR HIGH-PRESSURE

SPECTROSCOPIC INVESTIGATIONS

by

John Elliott Bedenbaugh

Approved: _____
Jochen Lauterbach, Ph.D.
Professor in charge of thesis on behalf of the Advisory Committee

Approved: _____
Norman J. Wagner, Ph.D.
Chair of the Department of Chemical Engineering

Approved: _____
Michael J. Chajes, Ph.D.
Dean of the College of Engineering

Approved: _____
Debra Hess Norris, M.S.
Vice Provost for Graduate and Professional Education

I would also like to thank the University of South Carolina for being such a big part of my life.

Most importantly, I would like to thank my family. In particular, I am grateful to my mother, Allyn, for her steadfast support and encouragement. I am also thankful to my brother, James, who makes any trip home very enjoyable. I would like to dedicate this thesis to my father, Don, and wish that he were able to experience its completion.

TABLE OF CONTENTS

LIST OF FIGURES

viii

ABSTRACT

In molecular-level catalytic investigations, discrepancies that exist between surface science observations under ultra-high vacuum (UHV) conditions and industrial catalytic performance at higher pressures are referred to as the "pressure gap." For example, changes in the population of adsorption sites and variation in reaction mechanisms on catalyst surfaces have been observed as pressure increases above UHV conditions. This work addresses this pressure issue through the investigation of surface adsorption behavior of model catalytic systems over the range from UHV to atmospheric pressures using polarization modulation infrared reflection absorption spectroscopy (PM-IRAS). Likewise, a "materials gap" exists between single crystal surfaces and the supported nanoparticle catalysts used industrially. This work also includes preliminary investigations exploring the use of the reverse micelle technique for catalyst synthesis in order to produce nanoparticles with well-controlled dispersion.

Adsorption of CO on Pt(100) was investigated at elevated pressures using PM-IRAS measurements. At sample temperatures of 325 K, a linear C-O stretch ($\sim$2090 cm^{-1}) was observed. Peak sharpening and a frequency shift were observed for this CO adsorption band at higher pressures. At 325 K, the frequency shift increased with exposures between 1 and 200 Torr CO up to 6.3 cm^{-1}. The full width half maximum of the IR band was observed to decrease by 27% over the same range. These results suggest that dipole-dipole coupling effects play an important role in understanding the surface adsorption behavior in this system at higher pressures.

A dipole-coupling model was applied to these experimental results. The model predicted CO surface coverages on the Pt(100) surface increasing from ~0.7 at 1 Torr CO to ~0.95 at 200 Torr CO. These results indicate that at higher pressures the CO surface coverage on Pt(100) is much greater than similar measurements obtained under UHV conditions. The predicted increases in surface coverage at higher pressures were verified through analysis of the integrated peak areas of the measured absorption bands. The calculated areas were observed to increase by up to 50% in magnitude over the pressure range from 1 Torr CO to 200 Torr CO. Measurements obtained during reduction from a high-pressure environment indicate that high-pressure adsorption behavior is a mix of reversible and irreversible processes.

Measured PM-IRAS spectra exhibit significant broadening and decreasing frequency with increasing sample temperature. These effects are consistent with phonon dephasing models for adsorbed molecules. Above certain sample temperatures, the absorption band associated with adsorbed CO is no longer observed in the measured spectra. This is attributed to CO dissociation at higher sample temperatures, resulting in carbon contamination of the Pt(100) surface. Subsequent spectra obtained after exposure of the system to oxidative conditions reveal the return of the absorption band corresponding to adsorbed CO. Temperature programmed desorption (TPD) measurements also corroborate this finding by excluding desorption as a likely cause of the loss of the CO band. Adsorbed CO measured in a CO oxidation reaction environment exhibit reversible adsorption/desorption processes around CO desorption temperatures.

In parallel to the above high-pressure studies, initial steps toward overcoming the materials gap were taken through the synthesis of Ru nanoparticles

using the reverse micelle synthesis technique. Reverse micelles were created using a microemulsion consisting of butyl ammonium laurate-water-hexanes. Dynamic Light Scattering was used to characterize the reverse micelles, which exhibited tunable sizes ranging from 5 to 30 nm depending on the molar water-to-butyl ammonium laurate ratio used. Reverse micelles having a diameter of 6 nm were then used to produce Ru nanoparticles from a $RuCl_3$ precursor solution. The resulting Ru particles had a diameter of ~3 nm, as determined from Small-Angle X-ray Scattering measurements. These results are a promising first step towards the goal of examining well-controlled nanoparticle catalysts over a wide range of pressure conditions using PM-IRAS. This approach has the potential to bridge both the pressure and materials gaps, allowing for significant improvements in the comparisons of model catalytic investigations with industrial catalytic performance.

Chapter 1

INTRODUCTION

1.1   Motivation

Molecular-level understanding and control of the active sites of a catalyst are principal objectives of heterogeneous catalysis research [1]. Molecular-level catalytic investigations have traditionally been performed using model catalysts consisting of single crystal surfaces under ultra-high vacuum (UHV) conditions [2]. However, discrepancies can exist between surface science observations in UHV conditions and industrial catalytic performance at higher pressures. For example, changes in the population of adsorption sites and variation in reaction mechanisms on catalyst surfaces have been observed as pressure increases above UHV conditions [3, 4]. This limitation, known as the "pressure gap," hinders detailed comparisons between model and industrial catalysts [5]. In addition, differences in catalytic performance that arise between single crystal surfaces and supported nanoparticles, which more closely mimic industrial catalysts, are known as the "materials gap." This work addresses the pressure issue through the investigation of model catalytic systems over the range from UHV to atmospheric pressures. In parallel, this work seeks to develop methods for the synthesis and investigation of supported nanoparticle catalysts at conditions up to atmospheric pressures.

The investigation of model catalytic systems can be effectively accomplished using vibrational spectroscopic techniques. Vibrational spectroscopy of

adsorbates was originally investigated by Eischens, who studied the adsorption of small molecules on supported metal catalysts [6]. An infrared reflection technique was developed for studying adsorbates on single crystal surfaces based on the pioneering calculations of Greenler, who derived optimal angles of incidence for the experiment [7]. Using vibrational spectroscopic techniques, it is possible to obtain information on surface adsorption sites as well as orientation of adsorbed molecules [8]. These techniques allow for molecular-level catalytic investigations of adsorption phenomena on well-defined single crystal surfaces. In the field of vibrational spectroscopy, electron-based techniques work well under UHV conditions. One example is electron energy loss spectroscopy (EELS), in which low energy electrons are inelastically scattered from a surface. The reflected electrons that excite vibrational modes in the adsorbate appear as discrete loss peaks in the resulting spectrum [8]. Vibrational spectroscopy allows for the precise measurement of position, form, intensity and coverage-dependent shift of vibrational bands, leading to information on the multiplicity of adsorption states, as well as adlayer growth, order-disorder phenomena and lateral interactions [8]. In comparison to EELS, such studies are best accomplished with infrared reflection absorption spectroscopy (IRAS), on account of its intrinsically high resolution [8]. Infrared reflection absorption spectroscopy (IRAS) is a technique where a beam of infrared radiation is reflected from the surface at near to grazing angles of incidence, giving rise to optical excitation of adsorbate modes [9].

However, traditional IRAS has limitations, as shown in Figure 1.1. In this figure, the number of gas phase molecules in 1 cm^3 volume is compared to the maximum number of molecules adsorbed on 1 cm^2 area of a single crystal surface over

a range of pressures. The IRAS technique is effective under UHV conditions, where

the number of adsorbed molecules on 1 cm^2 surface area greatly exceeds the number

of molecules in 1 cm^3 volume of gas. This is not true at pressures near atmospheric

and above, which reflect industrial operating conditions. At these higher pressures, the

number of molecules in the gas phase greatly exceeds the number of molecules

adsorbed on a surface. As a result, the number of potential infrared absorbers is much

greater in the gas phase, and the corresponding surface signal is often lost. The

inclusion of polarization modulation circumvents this limitation.
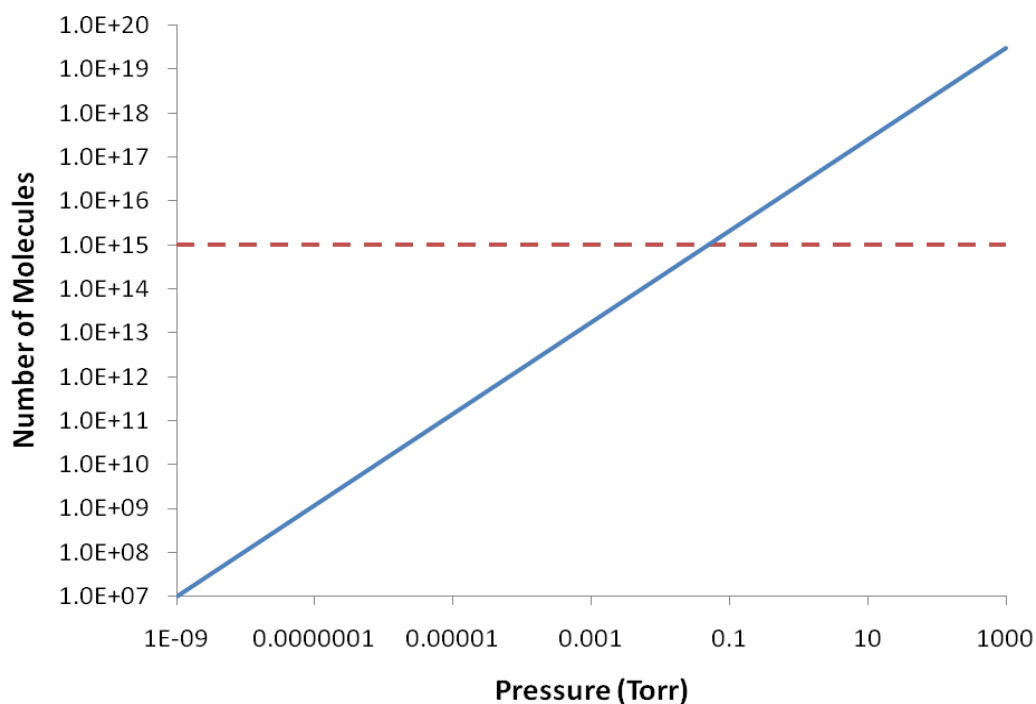
Figure 1.1. **Comparison between number of molecules in gas phase (1 cm^3 volume, blue/solid) and on surface (1 cm^2 area, red/dashed) over a range from UHV to near-ambient pressures.**

In order to study catalytic systems above UHV conditions, investigative techniques capable of functioning in higher pressure environments without undue interference from gas phase molecules are required. Unfortunately, as pressure increases above UHV conditions, the interference of molecules in the gas phase becomes increasingly significant and can prevent observation of surface species. Near atmospheric conditions, techniques designed for use in UHV conditions, such as EELS, are no longer effective. Consequently, several photon-based techniques have been developed for use in applications near atmospheric pressure.

A few techniques with high-pressure capability include infrared-visible (IR-vis) sum frequency generation (SFG), Raman spectroscopy, and polarization modulation infrared reflection absorption spectroscopy (PM-IRAS). These *in situ* vibrational spectroscopic techniques can be applied from UHV to ambient pressure and are thus able to interconnect classical surface science studies with catalysis at more industrially-relevant conditions through the study of adsorbed or reacting molecules on catalyst surfaces [1]. Nonlinear optical SFG spectroscopy is inherently interface specific and probes the surface directly because there is no gas phase SFG signal. In contrast, PM-IRAS allows for an accurate subtraction of the gas phase signal to yield surface vibrational spectra. The PM-IRAS technique has been used extensively for applications such as the study of thin polymer films, in situ electrode-electrolyte surface studies, and species at the air-water interface, among others. Properties of the PM-IRAS setup include an ability to detect sub-monolayer coverages and the ability to operate over a wide range of experimental conditions, spanning from ultra-high vacuum up to atmospheric conditions [10]. The polarization modulation allows for the removal of all aspects of the IR signal that do not pertain to surface

4

species, allowing for determination of the adsorption and reaction mechanisms occurring on a catalyst surface [11]. Compared to an IR-vis SFG setup, a PM-IRAS system is both relatively inexpensive and less experimentally intensive. A PM-IRAS system was constructed in our laboratory to enable analysis of adsorbed surface species at gas-solid interfaces from UHV to near-atmospheric pressure conditions through the study of surface vibrational spectra.

Previously, the PM-IRAS technique has been applied to a number of systems where there was a clear difference between adsorption behavior on surfaces under UHV conditions compared to higher pressures. One example is provided by Stacchiola, et al, from the study of carbon monoxide adsorbed on Pd(111) at 300 K [3]. This example shows how catalytic systems can behave differently at higher pressures and how experimental techniques capable of catalytic investigation at these higher pressures are crucial to studying these differences. Traditional IRAS identified a single absorption band at 1925 cm^{-1} associated with the adsorbed CO under UHV conditions, corresponding to adsorption in both face-centered-cubic (fcc) and hexagonal-close-packed (hcp) sites. However, at pressures above 1 Torr, IR absorption by gas phase molecules exceeded the signal associated with CO adsorbed on the surface. As a result, it became difficult to observe adsorbed surface species. This effect rendered the traditional IRAS technique ineffective at these higher pressures. To compensate for this, the researchers also applied PM-IRAS to this system. Using PM-IRAS, the same single peak at 1925 cm^{-1} was observed under UHV conditions. Above 1 Torr, however, interference from the gas phase signal was minimal using this technique, and the peaks associated with surface adsorption were still clearly visible at these higher pressures. With PM-IRAS, the researchers were

also able to observe a second peak at 2090 cm^{-1}, corresponding to CO adsorbed on atop sites on the Pd(111) surface. This second absorption band was not clearly visible using traditional IRAS due to the interference of the gas phase signal. However, application of the PM-IRAS technique allowed for successful measurement of both adsorption sites at higher pressures. This example illustrates how adsorbate-metal interactions can behave differently over the "pressure gap" through the fact that adsorption behavior can shift as pressure increases above well-controlled UHV conditions to reaction conditions near ambient pressure.

Similar to the palladium system described above, CO oxidation on platinum metals also exhibits a dependence on operating pressure and is a system of interest in this work. CO adsorption and oxidation on a Pt(100) single crystal surface are well-studied, but high-pressure spectroscopic investigations on this system remain lacking. CO adsorption and oxidation on Pt(100) provides a model system for applying PM-IRAS techniques to study catalytic systems over a range of pressures. This is discussed in more detail in the following section.

1.2   Carbon Monoxide Adsorption and Oxidation on Platinum

CO oxidation over platinum is a well-studied field in heterogeneous catalysis, first pioneered by Langmuir [12]. This system provides a model system for high-pressure vibrational spectroscopic studies in part due to the large dipole moment of the CO molecule as well as the simple nature of the reactants. Additionally, CO oxidation is industrially-relevant due to its importance in automotive catalysis, pollution control, and as a model of non-linear behavior in a catalytic system by exhibiting phenomena of general interest such as oscillations in reaction rate [13].

The CO oxidation reaction over platinum is shown in Equation 1.1 [14].

$$CO + \frac{1}{2}O_2 \rightarrow CO_2 \qquad (1.1)$$

$$CO(g) + * \Leftrightarrow CO* \qquad (1.1a)$$

$$O_2(g) + 2* \Leftrightarrow 2O* \qquad (1.1b)$$

$$CO* + O* \Leftrightarrow CO_2(g) + 2* \qquad (1.1c)$$
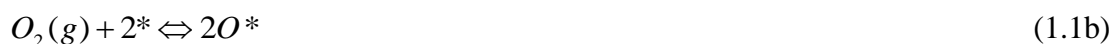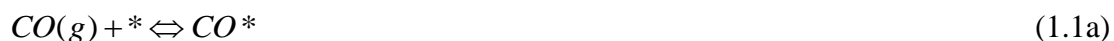
In this mechanism, the asterisk and CO* denote an adsorption site and adsorbed CO, respectively. Large differences in reaction behavior have been observed under UHV and industrially-relevant conditions, indicating a need for surface studies at high pressures. For example, the oscillatory behavior of the reaction is explained at high pressures by metal-oxide islands formation, which is not observed under UHV conditions [15].

The adsorption behavior of CO on platinum has taken on new interest recently due to the potential poisoning effects of CO on platinum anode catalysts in proton exchange membrane (PEM) fuel cells by CO contained in the reformed fuel gases. As a result, the adsorption of CO on platinum has been examined extensively from ultra-high vacuum conditions to elevated pressures [16]. Previous work has shown variation in the vibration bands associated with this adsorption indicating the system is sensitive to the environmental conditions. For instance, under ultra-high vacuum (UHV) conditions, the position of the linear C-O stretch on Pt(100) has been shown to shift to higher wavenumbers as CO exposure is increased [17]. This frequency shift corresponds with increasing CO surface coverage. The isotopic exchange rate of CO on Pt(111) has shown a strong dependence on the CO pressure, as well as significant variation in results obtained from nanoparticles as compared to

single-crystal surfaces, indicating a structure gap [16]. Specifically, the exchange rate at comparable CO pressures has been shown to be greater than 2 orders of magnitude faster for the Pt(111) surface than in experiments on Pt nanoparticles. This result indicates that investigations into this surface-sensitivity are necessary to develop a better understanding of this system.

The study of CO oxidation on platinum therefore provides the opportunity to apply both PM-IRAS and catalyst synthesis techniques to bridge the pressure and materials gaps in a single system. Another reaction that is significantly structure-sensitive and is less well understood than CO oxidation is the ammonia decomposition reaction, which will also be a model system for this work. The ammonia decomposition reaction provides motivation for developing a method of catalyst synthesis for producing well-controlled particles with low dispersion. Ultimately, this system can be investigated with PM-IRAS to gain valuable information about the reaction mechanism.

1.3 Hydrogen Production from Ammonia Decomposition

The U.S. Department of Energy has identified liquefied anhydrous ammonia, NH_3, as a potentially integral distribution and storage medium in a "hydrogen economy" [18]. Catalytic ammonia decomposition offers the potential for a clean, CO_x-free on-board supply of hydrogen for PEM fuel cells and other mobile applications. Ammonia produced through renewable means, such as solar or wind, offers the benefit of producing no greenhouse gases when consumed as a fuel. It offers several advantages as a hydrogen carrier, including high gravimetric hydrogen storage densities (1 kg H_2/8.5 L) and ease in liquefaction (P_{vap} = 9.2 bar at room temperature)

[19]. Ammonia can be transported and stored at much lower pressures than can pure hydrogen gas, as well. Two of the challenges that must be addressed for ammonia to become a viable hydrogen carrier include reductions in the temperature required for ammonia decomposition and improvements in the longevity and reliability of catalysts for ammonia decomposition [18].

Unfortunately, catalysts that are excellent for synthesizing ammonia have proven to be much less effective for decomposing ammonia to form hydrogen [20]. The ammonia decomposition reaction is endothermic, requiring temperatures above 500°C to achieve high conversion efficiencies. Making ammonia a viable hydrogen energy carrier would require the reduction of these catalytic decomposition temperatures nearer to PEM fuel cell operating temperatures, on the order of 200-300°C, without large sacrifices in ammonia conversion efficiencies [18]. A generally accepted catalytic mechanism for ammonia decomposition is shown in Equation 1.2, consisting of six reversible reactions.

$$NH_3 \rightarrow \frac{1}{2}N_2 + \frac{3}{2}H_2 \tag{1.2}$$

$$NH_3(g) + * \Leftrightarrow NH_3^* \tag{1.2a}$$

$$NH_3^* + * \Leftrightarrow NH_2^* + H^* \tag{1.2b}$$

$$NH_2^* + * \Leftrightarrow NH^* + H^* \tag{1.2c}$$

$$NH^* + * \Leftrightarrow N^* + H^* \tag{1.2d}$$

$$2H^* \Leftrightarrow H_2(g) + 2* \tag{1.2e}$$

$$2N^* \Leftrightarrow N_2(g) + 2* \tag{1.2f}$$

Conflicting evidence exists concerning the final step in this mechanism, with some research suggesting that nitrogen desorption occurs via a molecularly adsorbed species [21].

Further study of the ammonia decomposition reaction at high pressures is required due to lack of clarity concerning the reaction mechanism. Significant debate exists over the most abundant reactive intermediate (MARI) and the rate limiting step (RLS) for the ammonia decomposition reaction. Specifically, NH_2-H bond scission (Equation 1.2b), NH-H bond scission (Equation 1.2c), N-H bond scission (Equation 1.2d), and N-N recombinative desorption (Equation 1.2f) have each been proposed as the RLS for the decomposition mechanism [22, 23, 20, 24]. Debate exists over the MARI as well. Experiments on single crystals have reported that N* is the MARI, with negligible concentrations of H* [22]. However, other studies suggest that H* is the MARI, with N* present in some quantity [23]. As a result, further investigation of this system is necessary.

Because of these uncertainties, the ammonia decomposition reaction has received considerable recent attention. Researchers have demonstrated that single-metal catalysts, such as ruthenium, can exhibit high activity for ammonia decomposition [25]. Further increased activity for ammonia decomposition has been observed using ruthenium catalysts promoted with alkali and alkaline-earth metals [25, 26]. Also, differences arise when studies shift beyond model single crystal surfaces to supported nanoparticles. Researchers have demonstrated that particle size is a very important factor for achieving necessary activity increases in catalytic ammonia decomposition [27]. Ruthenium particles in the range of 2-5 nm have shown the highest activity for ammonia decomposition, with larger particles in this range being

the most active in terms of turnover frequency [27]. This is due to a maximum in the number of catalytically-active B5 sites present in nanoparticle catalysts in this size regime. In addition, bimetallic catalysts remain relatively untested for the application of ammonia decomposition. New bimetallic combinations of ruthenium and transition metals offer the potential to reduce the cost and temperature required for ammonia decomposition as compared to monometallic ruthenium. In light of the importance of investigating supported nanoparticles, particle size effects, and new bimetallic combinations, synthesis methods must be developed with these capabilities. Synthesis of nanoparticle catalysts via the reverse micelle technique provides a method for spanning the gap between model single crystal systems and industrial-grade catalysts.

1.4   Reverse Micelle Nanoparticle Synthesis

Preparation of catalysts using microemulsion – also known as "reverse micelle" – synthesis offers the advantages of effective control over particle size, due to the monodispersity of water droplets in the microemulsion solution. This method has been demonstrated to allow for small particle size distributions in the range of 2-50 nm [28]. Reverse micelle synthesis also allows for control of particle composition and morphology [28]. In this technique, a water-in-oil microemulsion is prepared by dissolving a small amount of an aqueous solution containing metal salts into an oil solution containing an amphiphile (surfactant). These surfactant molecules consist of hydrophilic heads and hydrophobic tails and become oriented so that small aqueous droplets are dispersed throughout the oil layer. These metal ion-containing aqueous droplets are known as "reverse micelles," and each of these droplets serves as a potential microreactor for catalyst synthesis. A reducing agent is added to the

11

microemulsion to stimulate particle synthesis in each droplet. The synthesis proceeds along two competing mechanisms. A nucleation process occurs for particle formation, while collisions between metal particles result in agglomeration [29]. Ultimately, a final uniform size distribution is reached [28].

The properties of a microemulsion can be finely tuned through variation of several parameters. Increasing the water concentration or decreasing the amount of surfactant added to solution will result in larger droplet sizes. This variation in the water-to-surfactant ratio, ω, has been shown to increase droplet size with increasing ω in a linear fashion [30]. Decreasing the amount of reducing agent added will also produce larger metal particles to a limiting value [29]. The presence of a large amount of reducing agent stimulates faster nucleation, resulting in smaller synthesized nanoparticles [29]. Variation of these parameters allows for the potential to develop a procedure for synthesizing nanoparticles of a specific size and distribution.

The advantages of the reverse micelle synthesis technique of effective control over particle size, composition, and morphology are especially significant for bimetallic applications. Studies of bimetallic systems have shown that bimetallic catalysts can be more active than either of the respective single metal catalysts [31, 32]. Bimetallic alloys also can exhibit improved selectivity, stability, and resistance to poisons in comparison to their pure metal counterparts [33]. This is often due to changes in the electronic or surface structure of the respective metal particles that make up the bimetallic catalyst [34, 35]. However, the surface structure and composition of these bimetallic alloys can vary with factors such as temperature, pressure, and presence of certain compounds. For this reason, bimetallic catalysts can exhibit very different properties when under reaction conditions, known as the "active

state" of the catalyst. These challenges require that catalyst examination be performed in situ, under reaction conditions.

1.5 Objectives and Thesis Scope

The goal of these investigations is to provide insight into the elementary steps of heterogeneous catalytic reactions with the objective of bridging both the pressure and materials gaps, allowing for significant improvements in the comparisons of model catalytic investigations with industrial catalytic performance. The approach to accomplish this involves application of surface vibrational spectroscopy using the PM-IRAS technique to explore surface adsorption behavior over a range of pressures from UHV to near-ambient conditions. This is combined with investigations bridging the materials gap through the synthesis of well-controlled nanoparticle catalysts using the reverse micelle method. Ultimately, combination of these parallel methods will allow for examination of well-controlled nanoparticle catalysts over a wide range of pressure conditions using PM-IRAS.

In this work, the PM-IRAS technique is applied to study the model system of CO adsorption and oxidation on a Pt(100) single crystal surface from UHV to near-atmospheric pressures. Using PM-IRAS, this work seeks to apply vibrational spectroscopy to gain valuable information about the adsorption and reaction sites on a catalyst surface. The PM-IRAS technique is also capable of identifying the predominant adsorbates present in a system, yielding valuable information about reaction mechanisms. With this information, it is possible to correlate new possible adsorption sites or variation in adsorption behavior to different reactivity over a range of pressures. In addition to the PM-IRAS investigations, the reverse micelle catalyst

synthesis technique is studied to explore the synthesis of ruthenium nanoparticles with well-controlled size dispersion. This work aims to explore the ability of the reverse micelle method to tune catalyst particle size in order to produce carefully controlled catalyst particles within a desired narrow size range.

This thesis consists of four chapters, including the preceding introduction consisting of motivation and background information in Chapter 1. In Chapter 2, the experimental equipment, methods, and techniques applied in this work are detailed. The high-pressure adsorption behavior and oxidation of CO on a Pt(100) single crystal surface were investigated using PM-IRAS. These CO adsorption and oxidation results are presented in Chapter 3. Chapter 4 details work investigating the reverse micelle catalyst synthesis technique for the synthesis of Ru nanoparticles with well-controlled dispersion. Finally, Chapter 5 contains a summary of the important conclusions.

1.6 References

[1] Rupprechter, G., Weilach, C. *Nano Today* (2007) **2**, 20-29.

[2] Somorjai, G.A. *Chem. Rev.* (1996) **96**, 1223-1235.

[3] Stacchiola, D., Thompson, A.W., Kaltchev, M., Tysoe, W.T. *J. Vac. Sci. Technol. A* (2002) **20**, 2101-2105.

[4] Rupprechter, G. *Advances in Catalysis* (2007) **51**, 133.

[5] Goodman, D.W. *Chemical Reviews* (1995) **95**, 523.

[6] Eischens, R.P., Pliskin, W.A. *Advan. Catalysis* (1958) **10**, 1.

[7] Greenler, R.G. *The Journal of Chemical Physics* (1966) **44**, 310-315.

[8] Bradshaw, A.M. *Applications of Surface Science* (1982) **11/12**, 712-729.

[9] Bradshaw, A.M. *Surface Science* (1985) **158**, 624-627.

[10] Urakawa, A., Burgi, T., Schlapfer, H.-P., Baiker, A. *The J. of Chemical Physics* (2006) **124**, 054717.

[11] Wallace, W.T., Cai, Y., Chen, M.S., Goodman, D.W. *J. Phys. Chem. B* (2006) **110**, 6245-6249.

[12] Langmuir, I. *Trans. Faraday Soc.* (1922) **17**, 621.

[13] Imbihl, R., Ertl, G. *Chemical Reviews* (1995) **95**, 697.

[14] Daniel, C., Clarté, M.-O., Provendier, H., Van Veen, A.C., Schuurman, Y., Beccard, B.J., Mirodatos, C. *Comptes Rendus Chimie* (2009) **12**, 647-653.

[15] Hendriksen, B.L.M., Bobaru, S.C., Frenken, J.W.M. *Catalysis Today* (2005) **105**, 234-243.

[16] Andersen, M., Johansson, M., Chorkendorff, I. *J. Phys. Chem. B* (2005) **109**, 10285-10290.

[17] Martin, R., Gardner, P., Bradshaw, A.M. *Surface Science* (1995) **342**, 69-84.

[18]   Thomas, G., Parks, G. Washington, D.C.: United States Department of Energy, 2006.

[19]   Larminie, J., Dicks, A. Fuel Cell Systems Explained. Wiley, 2003.

[20]   Ganley, J.C., Thomas, F.S., Seebauer, E.G., Masel, R.I. *Catalysis Letters* (2004) **96**, 117-122.

[21]   Hinrichsen, O., Rosowski, F., Muhler, M., Ertl, G. In Froment, G.F. and Waugh, K.C., editors, Dynamics of Surfaces and Reaction Kinetics in Heterogeneous Catalysis, Elsevier Science (1997), p. 389.

[22]   Tsai, W., Weinberg, W.H. *J. Phys. Chem.* (1987) **91**, 5302.

[23]   Mhadeshwar, A.B., Kitchin, J.R., Barteau, M.A., Vlachos, D.G. *Catal. Lett.* (2004) **77**, 13.

[24]   Yin, S.F., Xu, B.Q., Ng, C.F., Au, C.T. *App. Catal. B* (2004) **48**, 237.

[25]   Rarog, W., Kowalczyk, Z., Sentek, J., Skladanowski, D., Szmigiel, D., Zielinski, J. *Applied Catalysis A* (2001) **208**, 213-216.

[26]   Sorensen, R.Z., Nielsen, L.J.E., Jensen, S., Hansen, O., Johannessen, T., Quaade, U., Christensen, C.H. *Catalysis Communications* (2005) **6**, 229-232.

[27]   Yin, S.-F., Zhang, Q.-H., Xu, B.-Q., Zhu, W.-X., Ng, C.-F., Au, C.-T. *J. of Catal.* (2004) **224**, 384-396.

[28]   Eriksson, S., Nylen, U., Rojas, S., Boutonnet, M. *Applied Catalysis A* (2004) **265**, 207-219.

[29]   Chen, D.-H., Wu, S.-H. *Chem. Mater.* (2000) **12**, 1354-1360.

[30]   Lisiecki, L., Pileni, M.P. *J. Am. Chem. Soc.* (1993) **115**, 3887.

[31]   Chen, Y., Nickel, U. *J. Chem. Soc. Faraday Transactions* (1993) **89**, 2479.

[32]   Toshima, N., Harada, M., Yamazaki, Y., Asakura, K. *J. Phys. Chem.* (1992) **96**, 9927-9933.

[33]   Saint-Lager, M.C., Jugnet, Y., Dolle, P., Piccolo, L., Baudoing-Savois, R., Bertolini, J.C., Bailly, A., Robach, O., Walker, C., Ferrer, S. *Surface Science* (2005) **587**, 229-235.

[34]   Caballero, G.E.R., Balbuena, P.B. *Molecular Simulation* (2006) **32**, 297-303.

[35]   Bloxham, L.H., Haq, S., Yugnet, Y., Bertolini, J.C., Raval, R. *Journal of Catalysis* (2004) **227**, 33-43.

Chapter 2

MATERIALS AND METHODS

2.1   Surface Analytical System

A surface analytical system consisting of an ultra-high vacuum (UHV) base chamber and a high pressure reaction cell capable of attaining a range of pressures from UHV to ambient conditions was designed for studies of heterogeneous catalytic reactions. This system allowed for *in situ* surface analysis under reaction conditions utilizing photon spectroscopic techniques and temperature programmed desorption. This two-level experimental setup is shown in Figure 2.1. The high pressure cell was equipped with a Bruker Equinox 55 spectrometer and external Mercury-Cadmium-Telluride (MCT) detector for FTIR spectroscopic measurements. The base chamber included an Ar-ion sputter gun (Omicron) for sample preparation and a quadrupole mass spectrometer (Hiden HAL IV RC) for residual gas analysis and the measurement of temperature programmed desorption spectra.

The high pressure cell was separated from the base chamber by a gate valve (MDC 300004), which allowed the base chamber to retain ultra-high vacuum conditions while the high pressure cell was pressurized. Gases could be introduced to either or both chambers, via a leak valve in the lower chamber and a gate valve in the upper chamber. In addition, the two chambers could be pumped either separately or together. The lower chamber was constantly pumped by a turbomolecular pump (Leybold-Heraeus Turbotronic NT 150/360), which was also capable of pumping the

high pressure cell when the gate valve was open. The upper chamber was equipped with a separate turbomolecular pump (Varian) for when it was desired to pump each chamber separately. A three-dimensional translational stage provided an *in situ* sample transfer mechanism between the two levels.
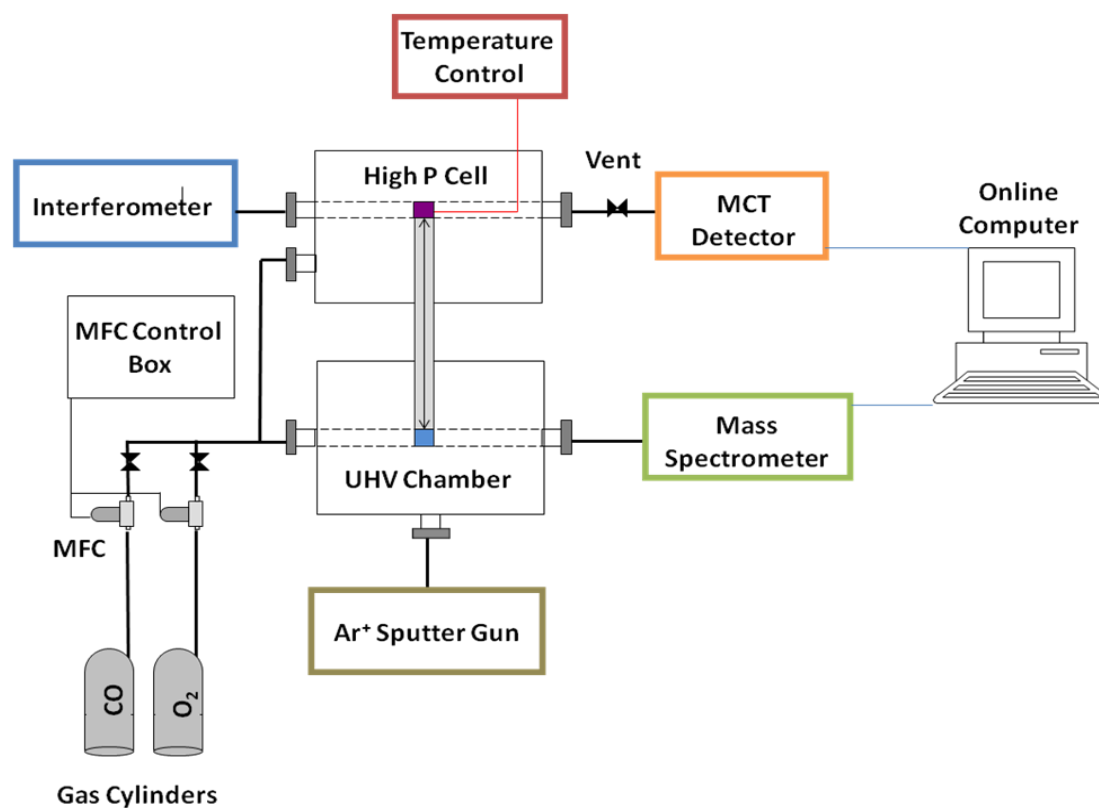
Figure 2.1.   Schematic of the two-level surface analytical system.

2.2   High Pressure Reaction Cell

The high pressure reaction cell was designed according to several constraints. Specifically, minimizing the cell volume offers several advantages, including reductions in the impurities desorbing from reactor walls, pump throughput requirements, and volume of gases required to pressurize the cell, as well as improved reactor mixing properties [1]. The design allowed the sample to be easily transferred between the reaction cell and the UHV base chamber for pre- and post-reaction surface analysis. In addition, since the reaction cell was used to perform infrared spectroscopic measurements, the cell geometry allowed for input and output of the infrared light source through KBr windows (International Crystal Laboratories 0002C-175) sealed by matching Buna O-rings.

When the gate valve separating the high pressure cell from the base chamber was closed, the mechanism for pressurizing the reaction cell could be used. A key valve opened up the high pressure cell to both an orifice valve connected to a roughing pump, as well as a valve connected to the Varian turbo pump. The orifice valve served a dual purpose, providing both a means to slowly evacuate the chamber at higher pressures as well as a safety feature preventing over-pressurization of the cell above atmospheric conditions. This was due to the fact that the orifice valve was rated to evacuate gas species faster than new species could be admitted to the chamber at atmospheric pressure. The high pressure cell could be valved off from not only the base chamber but also all pumping equipment in order to sustain a constant pressure environment within the reaction cell.

2.3   Sample Preparation

A Pt(100) single crystal was vertically mounted inside the chamber using a three-dimensional translational stage (MDC PSMA-1512) and rod extending from the translational stage into the reaction system. The translational stage allowed for manipulation of the sample ±0.5 in. from the centerpoint in the horizontal axes and provided up to 12 in. of travel in the vertical axis using compressible, flexible copper bellows. Two Ta wires were spot welded to the back of the sample and used to suspend the single crystal from a copper sample holder that was electrically isolated from the rest of the internal system by ceramic pieces. Insulated copper ribbon connecting external electrical feedthroughs with the sample holder allowed the sample to be resistively heated using a power supply (Lambda) by passing current through the tantalum wires, such that temperatures up to 1500 K could be maintained. The hollow mounting rod allowed for the introduction of liquid nitrogen near the sample for cooling. A type K thermocouple was also spot welded to the back of the sample and used to monitor sample temperature. Heating and cooling were computer controlled within ±0.5 K. A key advantage of the setup was that the thermocouple was in direct contact with the sample, providing exact measurement of the sample temperature. Similar systems often estimate sample temperature by using a thermocouple connected near the sample, for example to the sample holder, or by pyrometry [2]. The temperature of the sample holder is often much different from that of the sample, which can lead to inaccurate readings.

Prior to experiments, a clean surface was prepared with repeated cycles of three steps. The first step consisted of annealing the Pt(100) single crystal at ~1300 K for a period of ten minutes. The sample was then sputtered with Ar^+ ions under 2 x 10^{-5} mbar Ar for ten minutes. The final step involved oxidizing at 1050 K in 10^{-6} Torr

O_2 for fifteen minutes to remove surface carbon. When the sample was badly contaminated, this procedure was repeated until the surface was shown to be reactive. Sample cleanliness was checked via testing of the surface reactivity of the Pt(100) single crystal for the CO oxidation reaction before performing any experiments. In these reactivity experiments, the sample was heated to 473 K in 10^{-4} Torr O_2. A mixture of 74% O_2/26% CO by volume was then cycled into the chamber, and the production of CO_2 was monitored. A sample mass spectrometer signal (Faraday detector) for a clean, reactive surface is shown in Figure 2.2, exhibiting characteristic spikes for CO_2 production coincident with the introduction of CO into the system. Sample cleanliness was checked daily before conducting experiments as well as at the conclusion of any cleaning cycles. After each experiment, the sample was reacted in the presence of CO and O_2 to confirm the presence of a clean, reactive surface.
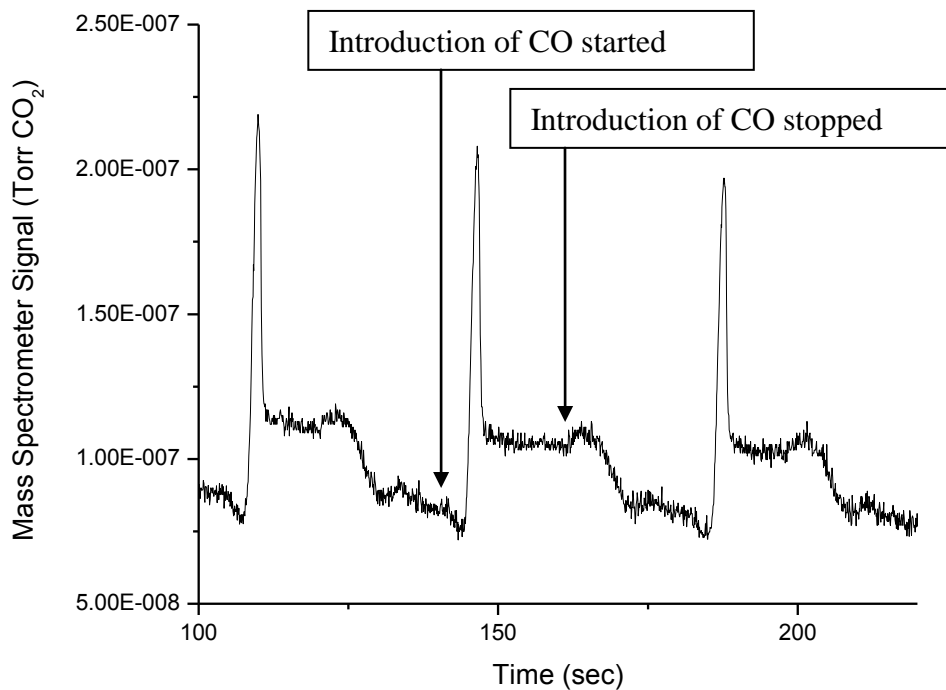
Figure 2.2. **Surface reactivity test for sample cleanliness using CO oxidation experiment on Pt(100) surface at 473 K and 10^{-4} Torr.**

2.4   Polarization Modulation Infrared Reflection Absorption Spectroscopy

As introduced in Chapter 1, infrared reflection absorption spectroscopy (IRAS) is a technique where a beam of infrared radiation is reflected from a sample surface at near to grazing angles of incidence, giving rise to optical excitation of adsorbate modes [3]. This technique is designed to take advantage of what is known as the surface selection rule. A molecule with a dynamic dipole moment that adsorbs onto a surface causes an image dipole to form in the surface that mirrors the dipole of

the adsorbed molecule, as shown in Figure 2.3. If the dipole of the adsorbed molecule is oriented in the plane of the surface, the addition of the image dipole produces no net dipole in the adsorbate-surface interaction. If the dipole of the adsorbed molecule is oriented perpendicular to the plane of the surface, however, the image dipole enhances the net dipole of the adsorbate by a factor of two. IRAS takes advantage of the fact that perpendicularly-adsorbed species absorb infrared light in order to yield surface vibrational spectra. However, as discussed in Chapter 1, IRAS is rendered ineffective at pressures above UHV conditions due to interference from gas phase molecules. The inclusion of polarization modulation (PM) circumvents this limitation.

The reflectance of light from a flat surface is governed by the Fresnel equations. The reflectances of incident radiation whose electric field is polarized parallel, R_p, or perpendicular, R_s, to the plane of incidence is shown in Equations 2.1 and 2.2.

$$R_p = \frac{\tan^2(\theta - \theta')}{\tan^2(\theta + \theta')} \tag{2.1}$$

$$R_s = \frac{\sin^2(\theta - \theta')}{\sin^2(\theta + \theta')} \tag{2.2}$$

In these equations, θ refers to the angle of incidence of the radiation, while θ' is the angle of refraction inside the material. The values of the absorption factor for light polarized perpendicular to the plane of incidence are smaller than those for light polarized parallel to the plane of incidence by as much as a factor of 10^5 [4].
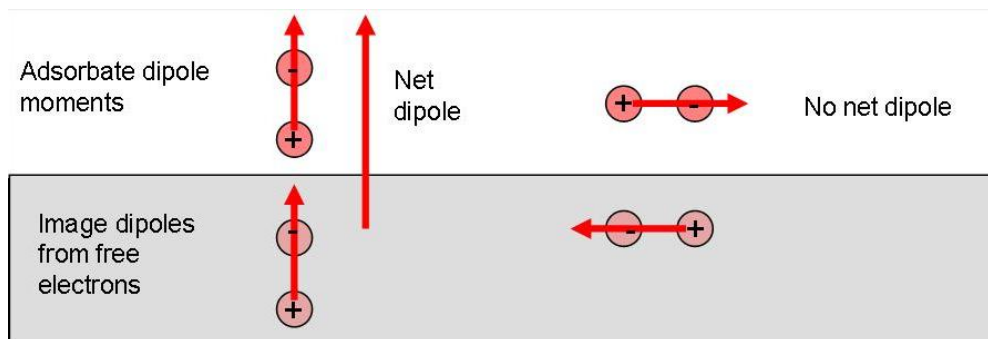
Figure 2.3.   Surface selection rule for adsorbed molecules.

The operational principle of the PM-IRAS technique is the modulation of a linearly polarized infrared beam into both a *p*-polarized beam and *s*-polarized beam, constituting two perpendicular polarization states of light as shown in Figure 2.4. According to the surface selection rules of reflected infrared radiation [5], *p*-polarized light, which oscillates with an electric field vector parallel to the plane of incidence, is absorbed by both gas phase species and surface species with a dynamic dipole moment perpendicular to the plane of the surface. In contrast, *s*-polarized light, which oscillates with an electric field vector perpendicular to the plane of incidence, is only absorbed by gas phase species. The difference between spectra obtained with *p*-polarized and *s*-polarized light therefore contains information yielding the surface vibrational spectra, virtually independent of the environmental conditions.
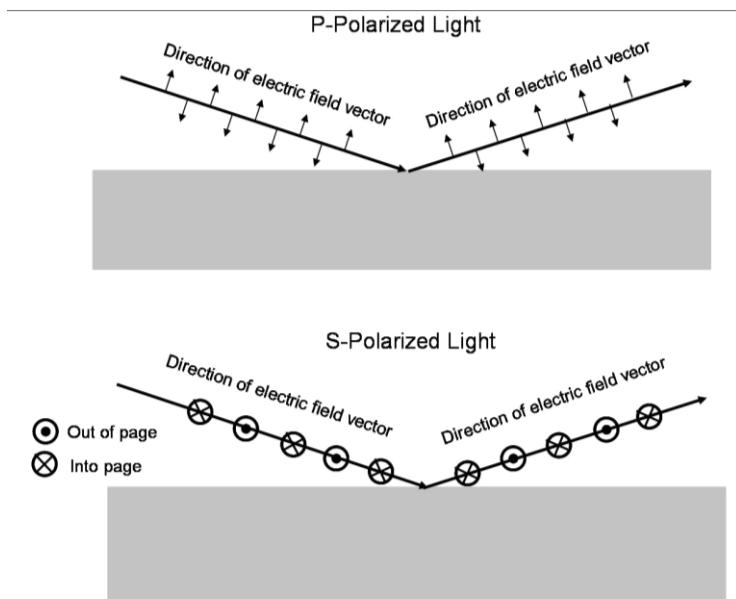
Figure 2.4.   Electric field vectors of incident infrared radiation.

Polarization modulation infrared reflection absorption spectroscopy (PM-IRAS) measurements were conducted within the high pressure reaction cell and could accommodate a range of pressures from UHV to atmospheric conditions. The polarization modulation optics and the IR spectrometer were located on a vibrationally-isolated optical top with pneumatic legs (Thorlabs) and purged with dry, CO_2-free compressed air (Parker Whatman 75-62 FTIR purge gas generator). Figure 2.5 shows a schematic of the PM-IRAS setup, including the infrared beam path as well as the electronics sampling layout. The collimated IR beam exited the external window of the interferometer and was reflected by two Au-plated mirrors, the second of which focused the beam with a focal point coincident with the sample position. After reflection from the mirrors, the IR beam passed through a wire-grid polarizer (Reflex Analytical Al/KRS-5), so that the transmitted IR radiation from the polarizer

26

had only a *p*-polarized electric field vector. The linearly-polarized IR beam then

passed through a photoelastic modulation (PEM) optical head (II/ZS50, 50 kHz, Hinds

Instruments) with a zinc selenide crystal aligned 45° from the surface normal. The

PEM was capable of shifting the polarization of the IR beam by 90° and could rapidly

modulate between the *s*-polarization and *p*-polarization states of light. The infrared

beam entered the high pressure cell through a KBr window and impinged on the

sample at an incidence angle of ~85° from the surface normal. The beam was reflected

off of the sample surface and exited the high pressure cell through another KBr

window. The IR beam reflected from the surface was collected by a focusing mirror

onto a liquid nitrogen-cooled, narrow-band mercury-cadmium-telluride (MCT) IR

detector. The signals from the PEM and MCT detector were inputs to a lock-in

amplifier, which output the resulting surface spectra to the computer for data analysis.
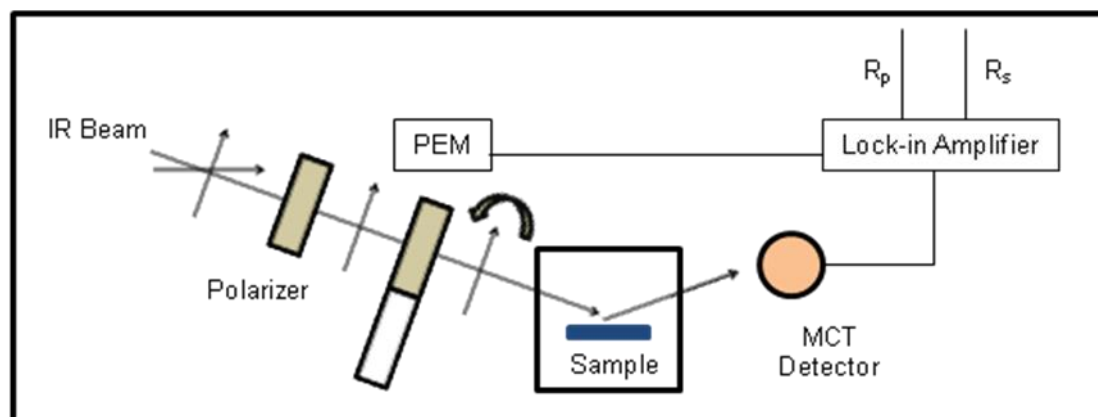

Figure 2.5.   Schematic of PM-IRAS system.

The separated signals from the lock-in amplifier were ratioed to yield the

final surface spectra using OPUS™ spectroscopic software. This was accomplished

according to the following procedure. In principle, the difference between the collected spectra corresponding to *p*-polarization and *s*-polarization was determined and normalized over the sum of the two, according to Equation 2.3.

$$\frac{\Delta R}{R} = \frac{|R_p - R_s|}{R_p + R_s}$$

(2.3)

In reality, the differential and sum spectra were dependent upon the PEM used to modulate the polarization, optical components located in the setup, and sensitivity enhancement by the lock-in amplifier [6]. The impact of these system parameters on the measured spectra is detailed in the following section. In a general PM-IRAS experiment on any sample layer of thickness *d*, the signal at the detector output can be electronically split into two parts. The first part, the modified sum spectra shown in Equation 2.4, is simply modulated at the Fourier frequencies ω_i induced by the moving mirror of the FT-IR spectrometer [7].

$$I_{DC} = C_{DC} I_0^p(\omega_i) \times \left[\left(R_p(d) + R_s(d) \right) + \left(R_p(d) - R_s(d) \right) \cdot J_0(\varphi_0) \right]$$

(2.4)

The second part, the modified differential spectra shown in Equation 2.5, has a double modulation at the Fourier frequencies ω_i and at the much higher frequency ω_m induced by the photoelastic modulator [7].

$$I_{AC} = C_{AC} I_0^p(\omega_i) \times \left[\left(R_p(d) - R_s(d) \right) \cdot J_2(\varphi_0) \cdot \cos(2\omega_m t) \right]$$

(2.5)

In these equations, $I_0^p(\omega_i)$ is the intensity of the *p*-polarized infrared radiation of frequency ω_i at the output of the polarizer before the PEM, R_p and R_s are the polarized reflectances of the film/substrate system, and J_2 and J_0 are the second- and zero-order Bessel function of the maximum dephasing φ_0 introduced by the photoelastic modulator.

After demodulation of the I_{AC} signal with a lock-in amplifier, the ratio of these two parts gives the "theoretical" PM-IRAS signal S(d) shown in Equation 2.6 [7].

$$S(d) = \frac{I_{AC}}{I_{DC}} = \frac{g \cdot \left|\left(R_p(d) - R_s(d)\right) \cdot J_2(\varphi_0)\right|}{\left(R_p(d) + R_s(d)\right) + \left(R_p(d) - R_s(d)\right) \cdot J_0(\varphi_0)} \qquad (2.6)$$

In this equation, g is a constant accounting for the different gain and filtering occurring during the two-channel electronic processing. However, the experimental signal may be affected by the polarization dependence of the optical parts located between the PEM and the detector, such as multiple reflections inside the PEM, convergence of the beam, or preferential polarization produced by the window in front of the detector. As a result, an additional term γ must be included to account for the different overall responses C_p and C_s of the optoelectronic setup for the p and s polarizations. The final relation is shown in Equation 2.7, with $\gamma = C_p/C_s$ [7].

$$S(d) = \frac{I_{AC}}{I_{DC}} = \frac{g \cdot \left|\left(\gamma R_p(d) - R_s(d)\right) \cdot J_2(\varphi_0)\right|}{\left(\gamma R_p(d) + R_s(d)\right) + \left(\gamma R_p(d) - R_s(d)\right) \cdot J_0(\varphi_0)} \qquad (2.7)$$

The process of removing the gas phase contribution to yield surface vibrational spectra is illustrated in the following figures. For this exercise, CO was adsorbed onto Pt(100) at an adsorption temperature of 325 K and 50 Torr CO pressure. Figure 2.6 shows the difference spectrum, ΔR, between the signals associated with s-polarized and p-polarized light. This difference spectrum is then normalized over the sum of those two signals, R, which is shown in Figure 2.7. The result of this calculation is the spectrum associated with the surface species, with the signal associated with the gas phase contribution removed, as shown in Figure 2.8. It should be noted that in a traditional IRAS experiment, the surface vibrational spectrum would

29

not be visible at these conditions due to the surface signal being greatly exceeded and effectively obscured by the gas phase signal. The external purge boxes proved sufficient for removing significant quantities of water and CO_2 from the infrared beam path. Trace adsorption bands arising from atmospheric water and CO_2 are present in the unmodulated spectra, but they are removed in the PM-IRAS demodulated spectra. This process illustrates how the absorbance contributions from gas phase molecules can be subtracted through the use of rapid polarization modulation.
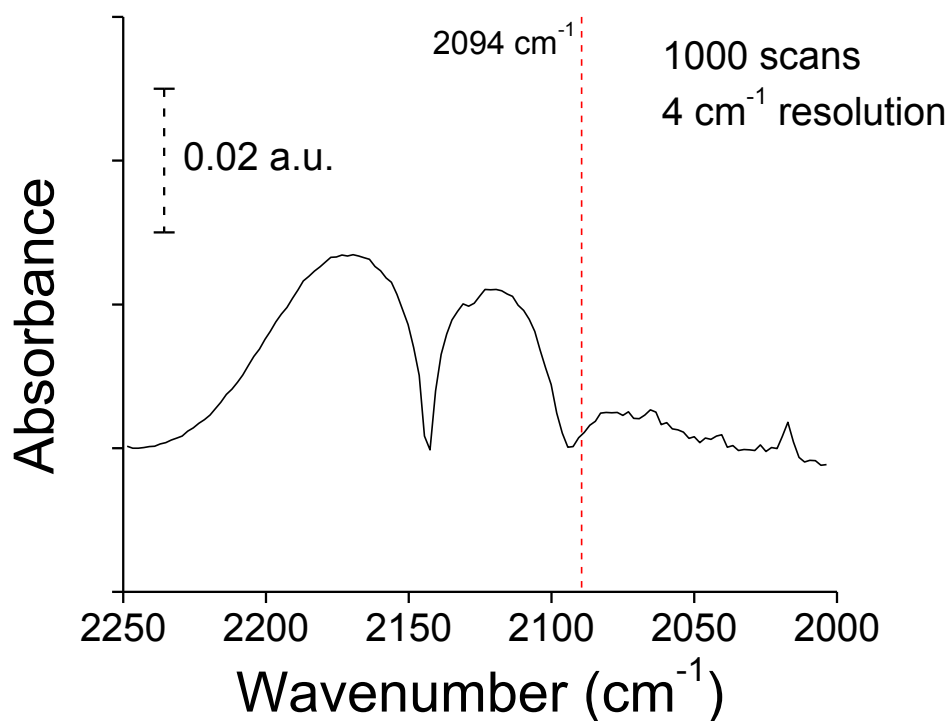
Figure 2.6. **Difference between R_p and R_s signals.**
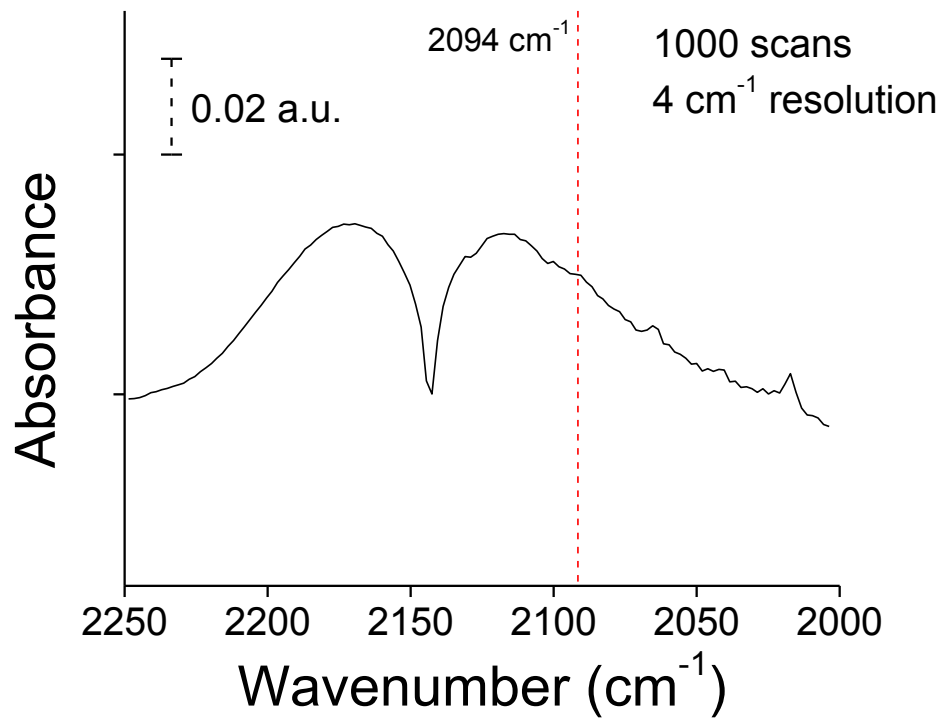
Figure 2.7.   Sum of R$_p$ and R$_s$ signals.
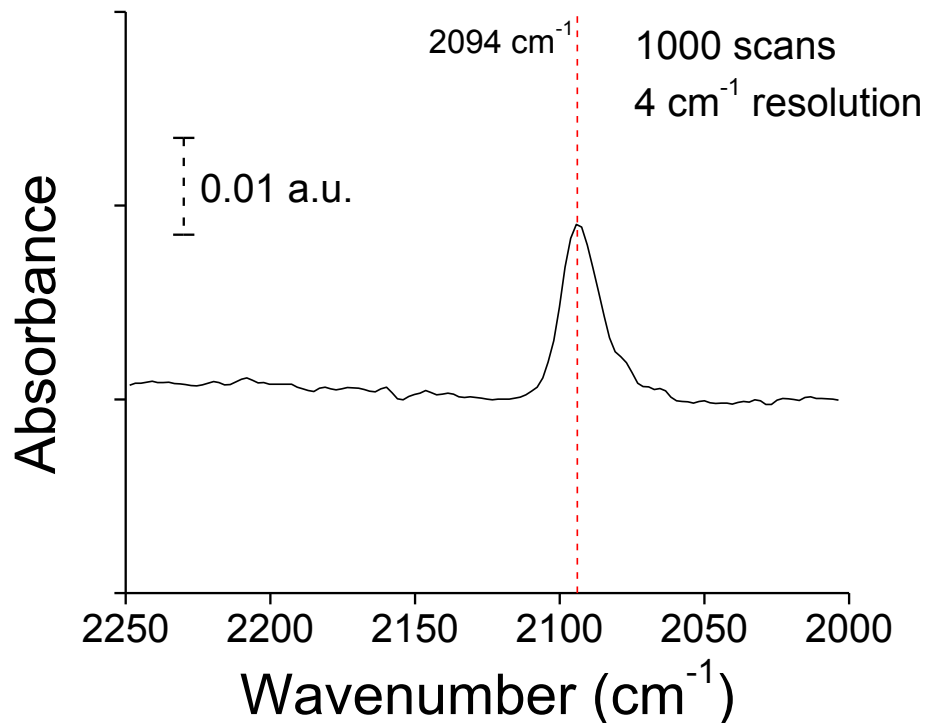
Figure 2.8.   Resulting surface spectra obtained with PM-IRAS.

2.5   CO Adsorption on Pt(100)

All experiments were carried out on a Pt(100) single crystal catalyst within the stainless steel, two-level ultra-high vacuum chamber described above. The base pressure in the system was below 5×10^{-9} Torr, so that the adsorption of gas from the ambient was negligible. The surface analytical system allowed for sample investigation using PM-IRAS over a large range of temperatures and environmental pressure conditions for both UHV and high-pressure studies. For these experiments, CO was adsorbed onto the Pt(100) surface at a specific adsorption temperature, T_{ads}.

For UHV studies, the sample could experience either a given exposure of CO or a constant pressure environment. For high pressure studies above 1 Torr, the sample was exposed to CO at a given constant pressure. The sample temperature and environmental pressure were easily varied using the heating and pressurization mechanisms described above. Upon adjustment, sample temperature and chamber pressure were allowed sufficient time to stabilize before experiments were conducted.

All of the IR spectra were recorded with a resolution of 4 cm^{-1} and represent the addition of 500 or 1000 scans to ensure satisfactory signal-to-noise ratios. Prior to acquiring each spectrum, a background spectrum was recorded as a reference. Gases were supplied to the system via 316 stainless steel tubing. The purity of the CO (Matheson, 99.998%) and O_2 (Matheson, 99.998%) gases were confirmed with the mass spectrometer.

2.6 Temperature Programmed Desorption

Temperature programmed desorption measurements were conducted in the UHV chamber described previously using a mass spectrometer to monitor molecules desorbed from the surface. The scanning electron multiplier (SEM) detector on the mass spectrometer was used to obtain thermal desorption spectra. The sample was heated by a linear temperature ramp in the line of sight of the mass spectrometer at a controlled heating rate of 2 K/sec to 3 K/sec. Hiden MASSoft™ software was used to monitor the presence of specific molecules in the system. For exposure experiments, samples were exposed to doses of adsorbates from 10 L to 6000 L at specific adsorption temperatures from 300 K to 500 K.

In a typical experiment, the Pt(100) sample would be held at a constant temperature, T_{ads}, typically well below CO desorption temperatures while CO was admitted to the system. The system was then allowed a brief time to pump down to the original vacuum conditions. The sample was then heated at a computer-controlled constant rate to temperatures sufficient to remove the adsorbed CO from the surface through desorption. Evolution of CO in the gas phase through desorption from the sample surface was monitored using the mass spectrometer in order to determine the desorption characteristics of the system.

2.7 References

[1] Campbell, C.T. *Advances in Catalysis* (1989) **36**, 1.

[2] Jachimowski, T.A., Lauterbach, J. *Review of Scientific Instruments* (1998) **69**, 2757-2761.

[3] Bradshaw, A.M. *Surface Science* (1985) **158**, 624-627.

[4] Greenler, R.G. *The Journal of Chemical Physics* (1966) **44**, 310-315.

[5] Hoffmann, F.M. *Surface Science Reports* (1983) **3**, 107.

[6] Urakawa, A., Burgi, T., Schlapfer, H.-P., Baiker, A. *The J. of Chemical Physics* (2006) **124**, 054717.

[7] Buffeteau, T., Desbat, B., Blaudez, D., Turlet, J.M. *Applied Spectroscopy* (2000) **54**, 1646-1650.

Chapter 3

ADSORPTION OF CO ON PT(100) INVESTIGATED WITH PM-IRAS

3.1 High-Pressure Adsorption of CO on Pt(100)

The high-pressure adsorption of CO on Pt(100) is studied as a model catalytic system for PM-IRAS measurements. The infrared spectra of CO adsorbed on Pt(100) at 325 K are shown for a range of pressures from 1 to 200 Torr CO in Figure 3.1. As can be seen, a single vibrational band is observed above ~2090 cm^{-1}, associated with the linear C-O stretch due to CO adsorbed on atop sites. On Pt(100), CO chemisorbs with the molecular axis perpendicular to the platinum surface with the carbon atom oriented toward the surface. A visual representation of this adsorbate-substrate system is included in Figure 3.2 [1]. No adsorbed CO was detected corresponding to bridge sites in this system. Instead, the adsorption of CO on atop sites on Pt(100) is observed over this entire pressure range. Infrared reflection absorption spectroscopy (IRAS) studies of this system under UHV conditions identify a single vibrational band at ~2067 cm^{-1} upon initial exposure of CO to the clean Pt(100) surface [2]. This band increases in both intensity and position with additional CO exposure. Little variation is observed in the linear C-O band above a pressure of 10^{-7} mbar CO, as the band position remains at ~2088 cm^{-1}.

The infrared spectra from Figure 3.1 can be divided into two separate pressure regimes. The lower-pressure regime (1-20 Torr CO) is shown in Figure 3.3. Over the range of pressures from 1 to 20 Torr CO, very little variation is observed in

the peak position or peak shape corresponding to this band. However, differences

arise within the higher-pressure regime (50-200 Torr CO), shown in Figure 3.4. As

pressure increases to 200 Torr CO, a marked shift in peak position to ~2095 cm^{-1} as

well as a sharpening of the absorption band are observed. The spectrum obtained in

the presence of 1 Torr CO is included in Figure 3.4 as a visual reference. The

observed variation in both peak position as well as bandwidth in terms of full width at

half maximum (FWHM) measurements are included in Figure 3.5 for the entire

pressure range.
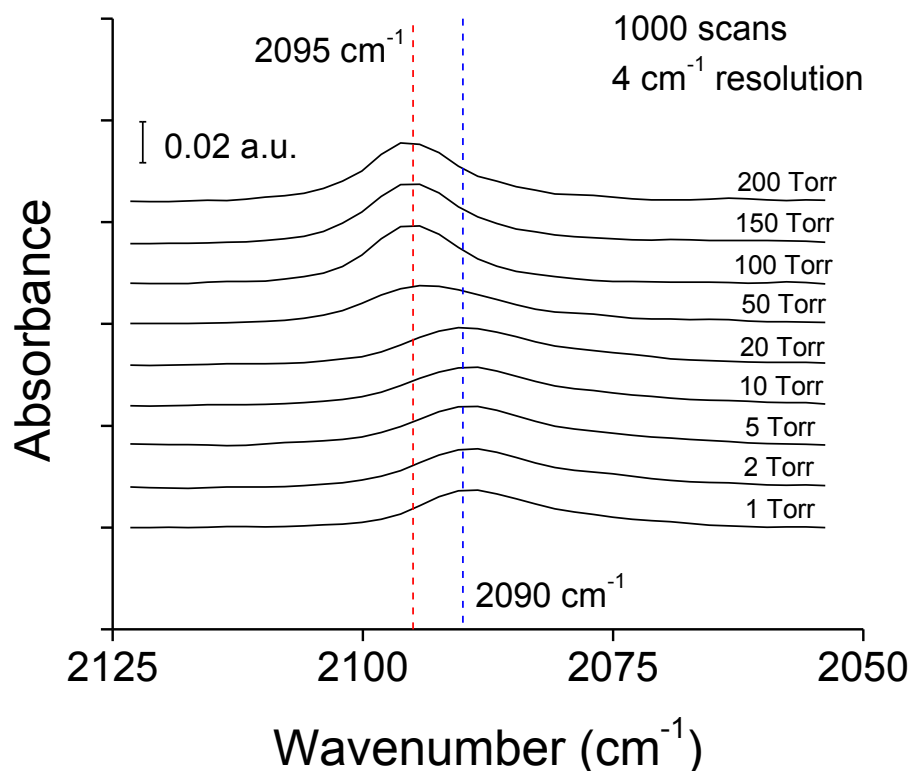
**Figure 3.1.   CO adsorbed on Pt(100) at 325 K, 1-200 Torr CO.**
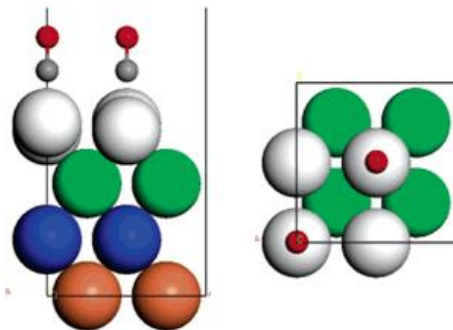
Figure 3.2. Side view [left] and top view [right] of CO molecules adsorbed on atop sites on Pt(100) [1].
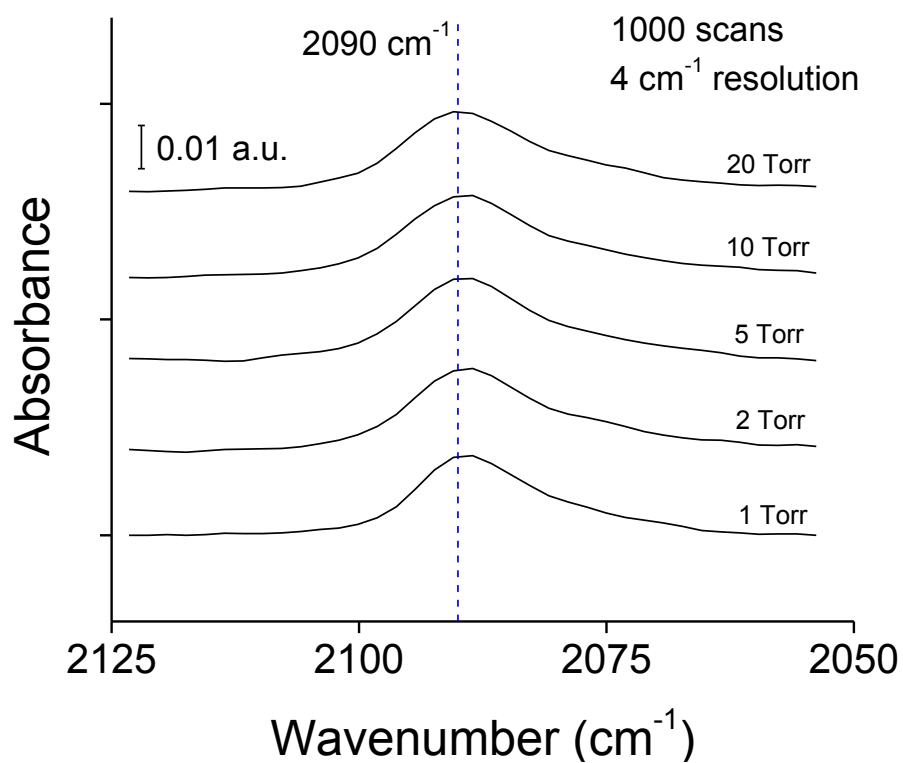
Figure 3.3 Linear C-O Stretch for CO Adsorbed on Pt(100), 1-20 Torr CO.
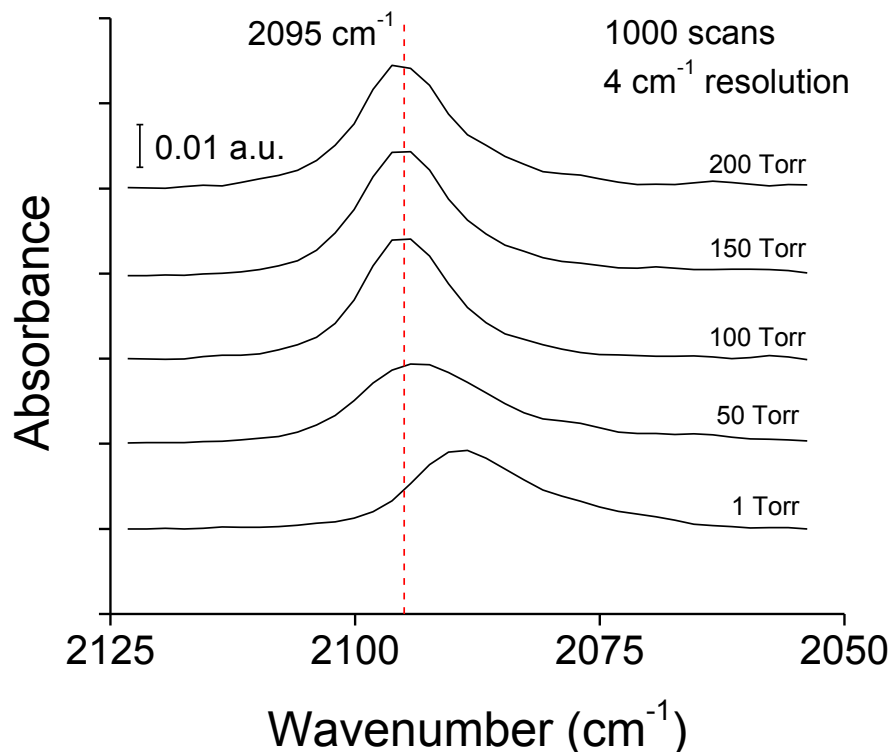
Figure 3.4   Linear C-O Stretch for CO Adsorbed on Pt(100), 50-200 Torr CO.
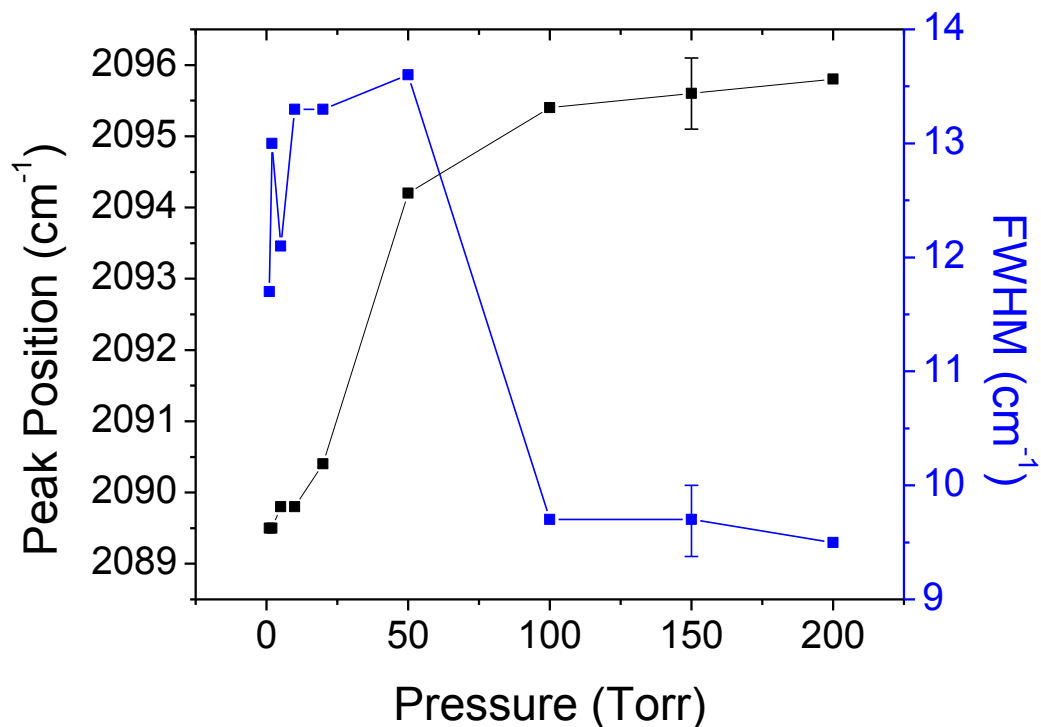
Figure 3.5   Peak Position and FWHM measurements for CO Adsorbed on Pt(100) at 325 K from 1-200 Torr CO.

The frequency of the observed IR absorption band exhibits an upward shift with increasing coverage caused by dipole-dipole coupling among the adsorbed CO molecules. This is illustrated in Figure 3.5, which shows the position of the peak maximum as a function of the CO pressure. Figure 3.5 also shows the corresponding linewidth measurements in terms of the full width at half maximum (FWHM) of the IR absorption bands. The frequency of the absorption band increases by more than 6 cm^{-1} over the range from 1 to 200 Torr CO. The shift in peak position of the linear C-O stretch of atop CO to higher wavenumbers is consistent with dipole-coupling models for increasing CO surface coverage. The decrease in the linewidth

measurements with increasing pressure is also explained through the contributions of dipole-coupling. Previous studies have shown that strong dipole-dipole coupling causes line narrowing with increasing coverage [3]. To investigate these effects, a dipole-coupling model is applied to these data.

The dipole-coupling model in this analysis is shown in Equations 3.1 and 3.2 [4]:

$$\frac{\omega}{\omega_s^2} = 1 + \frac{\Theta \alpha_v \Sigma_0}{1 + \Theta \alpha_e \Sigma_0} \tag{3.1}$$

$$\Sigma_0 = \sum_{i \neq j} \frac{1}{r_{ij}^3} + \frac{1}{\left| r_{ij} + 2d\hat{z} \right|^3} - \frac{12d^2}{\left| r_{ij} + 2d\hat{z} \right|^5} \tag{3.2}$$

According to Equation 3.1, the frequency of an absorption band, ω, with respect to the singleton frequency, ω_s, corresponding to an isolated CO molecule on the surface, is a function of the dipole sum Σ_0 of the adsorbate at complete coverage, and the adsorbate coverage, Θ. In addition, the electronic and vibronic polarizabilities, α_e and α_v, respectively, serve as fitting parameters. As shown in Equation 3.2, the value of Σ_0 is dependent on the distance between the center of the molecular dipole and the image plane of the surface, d, and the distance between dipoles in the plane of the surface, r_{ij}.

The dipole-coupling model described above is applied to examine the coverage-dependent frequency shift of the absorption band for these high-pressure experiments. Based on the model predictions, the dependence of absorption band frequency on coverage is shown in Figure 3.6. The model-predicted surface coverages for CO adsorbed on atop sites on Pt(100) at 325 K based on the experimental data are shown in Figure 3.7. For these calculations, the dipole sum was calculated for d = 1 Å. The singleton frequency for CO adsorbed on atop sites on Pt(100) used was $\omega_s =$

2067 cm^{-1}, selected from experimental data [2]. Based on previous estimation by

Scheffler, the electronic polarizability was chosen to be $\alpha_e = 2.54$ Å^3, corresponding to

the component of the polarizability tensor of the CO molecule parallel to the symmetry

axis of the molecule [5]. The best fit is obtained for vibronic polarizability $\alpha_v = 0.35$

Å^3. This value is consistent with estimation applied in previous CO dipole-dipole

coupling models [4].
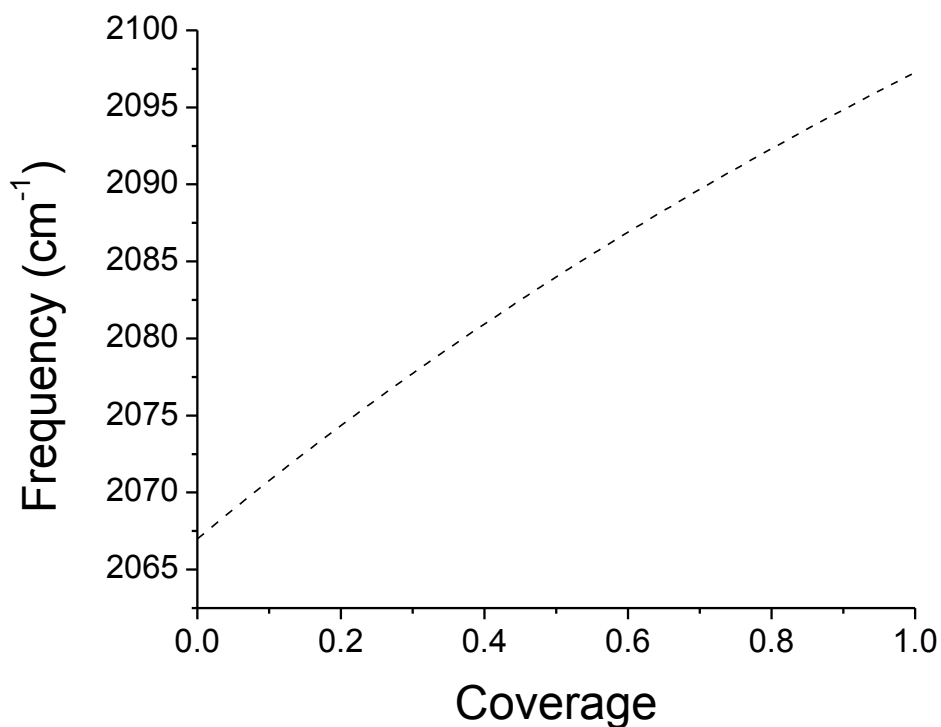
Figure 3.6. **Dipole-coupling model-predicted frequency shift with coverage for CO adsorbed on atop sites on Pt(100) at 325 K.**
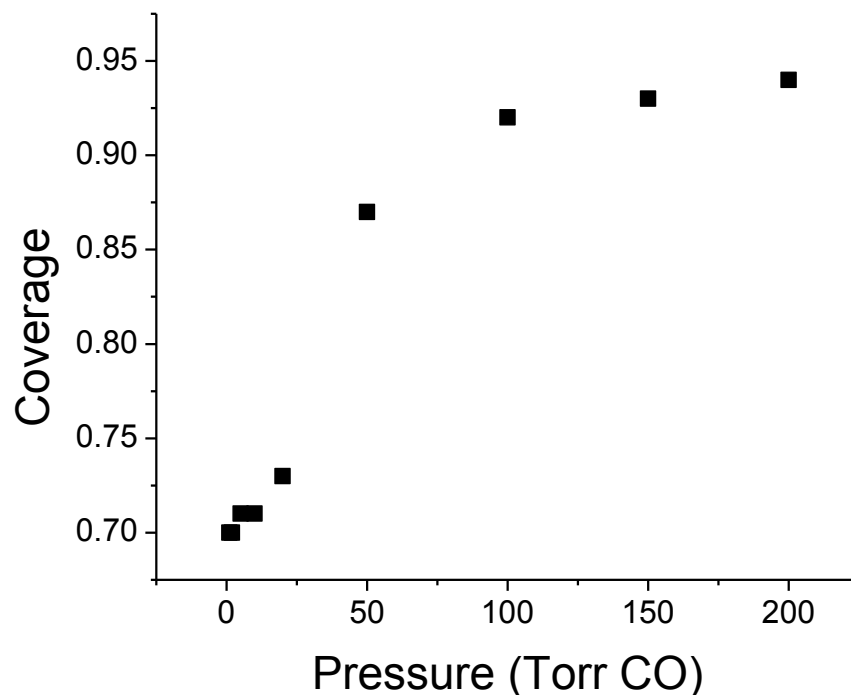
Figure 3.7.   Dipole-coupling model-predicted coverages for high pressure CO adsorption on Pt(100) at 325 K.

As can be seen in Figure 3.6, the frequency of the absorption band increases non-linearly with increasing surface coverage. Higher surface coverages are achieved as pressure increases. As more molecules adsorb to the surface, the dipole-coupling strength of the adsorbed molecules increases. This observation is consistent with high-pressure results obtained from CO adsorbed on other platinum surfaces [6]. As illustrated in Figure 3.7, the dipole-coupling model predicts surface coverages in the lower-pressure regime between 0.7 and 0.75. The predicted surface coverages then increase to greater than 0.9 in the higher-pressure regime for 100 Torr CO and above. The observed decrease in linewidth at these higher pressures can be explained by the

presence of very high surface coverages, leading to less inhomogeneity on the metal surface and a corresponding decrease in the linewidth of the absorption band. The predicted surface coverages achieved in these experiments are well above those measured for this system under UHV conditions. This result is an important first step in understanding differences in behavior of this system as experiments span the pressure gap from UHV to near-atmospheric conditions.

The model-predicted observation of increasing surface coverage at higher pressures is verified by calculation of the integrated peak areas of the observed absorption bands, as shown in Figure 3.8. The integrated peak areas are reported in terms of a relative ratio to the absorption of the 1 Torr CO system. The integrated peak area of the absorption bands for adsorbed CO shows a corresponding increase as pressure increases. A rapid increase in peak area is observed in the lower-pressure regime. At higher pressures, however, the IR absorption increases much less significantly. This effect can be attributed to a much smaller absorption per CO molecule due to dielectric screening caused by the electronic polarizability of the CO molecules [7]. There is an exception at 50 Torr CO, which is likely an artifact of the data analysis because it corresponds with the peak broadening at 50 Torr CO in the FWHM measurements in Fig. 3.5. The observed increases in integrated peak area support the idea that higher surface coverages are being achieved at these higher pressures, much greater than those that have been observed under UHV conditions.
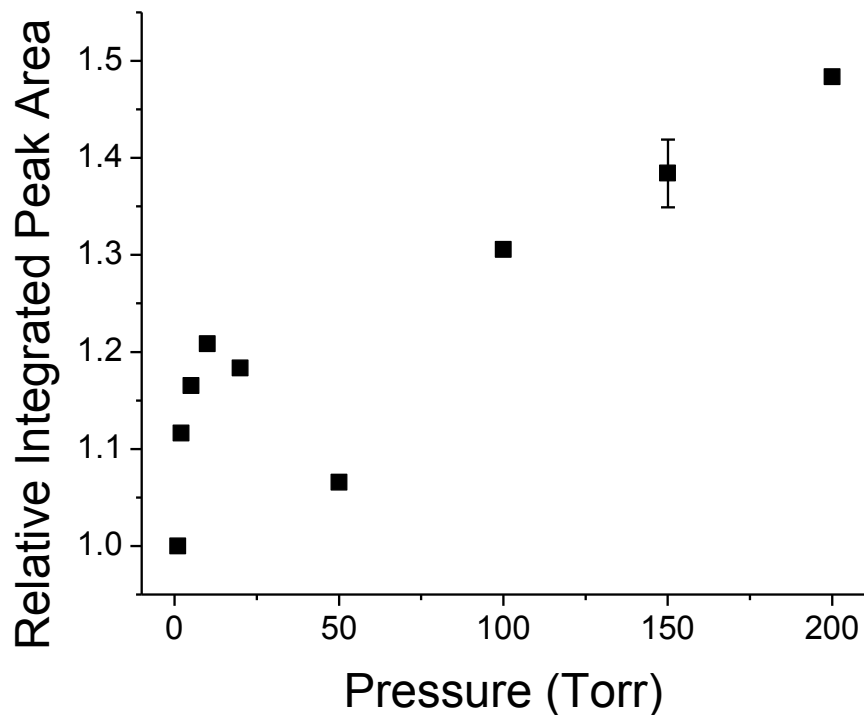
Figure 3.8. **Integrated peak areas of atop site absorption band for CO adsorbed on Pt(100) at 325 K over range of pressures from 1-200 Torr CO.**

The stability of the higher-pressure surface coverages was investigated experimentally to determine whether the surface coverage of adsorbed CO remains stable upon reduction of the pressure in the system. In this experiment, the reaction chamber pressure was reduced after pressurization to 200 Torr CO. PM-IRAS spectra were taken during the pressure increase from 10 to 200 Torr CO and then again afterwards at the reduced pressure state of 100 Torr CO. The integrated peak areas of the absorption bands in this experiment are shown in Figure 3.9. The integrated peak areas are reported in terms of a relative ratio to that of the 10 Torr CO system. It is found that the amount of CO adsorbed on the surface as measured by integrated peak

area after reducing the pressure to 100 Torr CO registers below that of the 200 Torr CO band but above the expected value for the lower pressure band. Instead, the amount of adsorbed CO on the surface is between the two positions, indicating a mix of reversible and irreversible adsorption characteristics as the system is exposed to increasing pressure conditions.
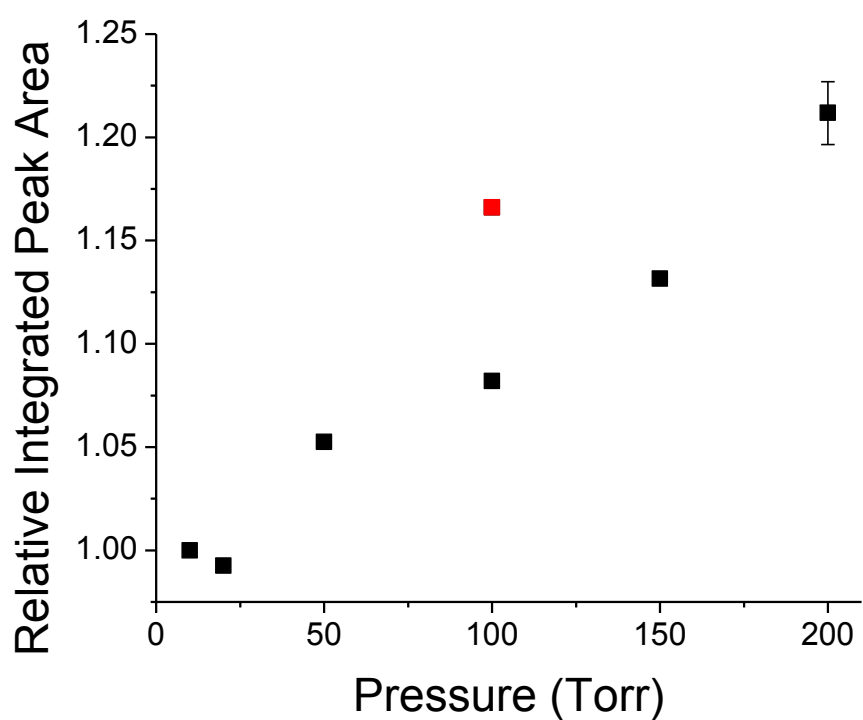

Figure 3.9.   CO Adsorbed on Pt(100) at 325 K for increasing (black) and decreasing (red) pressure measurements from 10-200 Torr CO.

3.2 Temperature-Dependent Adsorption of CO on Pt(100)

All of the results shown thus far were obtained for sample temperatures of 325 K. The CO oxidation reaction occurs at temperatures well above 325 K, however – at conditions closer to 450-500 K. Therefore, it is also important to study adsorption behavior at higher temperatures as well. Similarly to the pressure study above, variation in the sample temperature of the Pt(100) surface results in shifts in CO adsorption behavior. For a system at a constant pressure of 2 Torr CO, the infrared spectra of CO adsorbed on Pt(100) are shown for increasing temperature measurements from 325 K to 400 K in Figure 3.10. The CO molecules initially adsorbed to the surface at a temperature of 325 K, and then the surface was heated to higher temperatures. A slight shift in peak position to a lower frequency is observed as temperature increases. Additionally, peak broadening is observed in the higher temperature measurements as shown by the increase in FWHM measurements from 11.9 cm^{-1} at 325 K to 14.1 cm^{-1} at 375 K. At temperatures above 400 K, however, the observed CO peak is essentially removed.
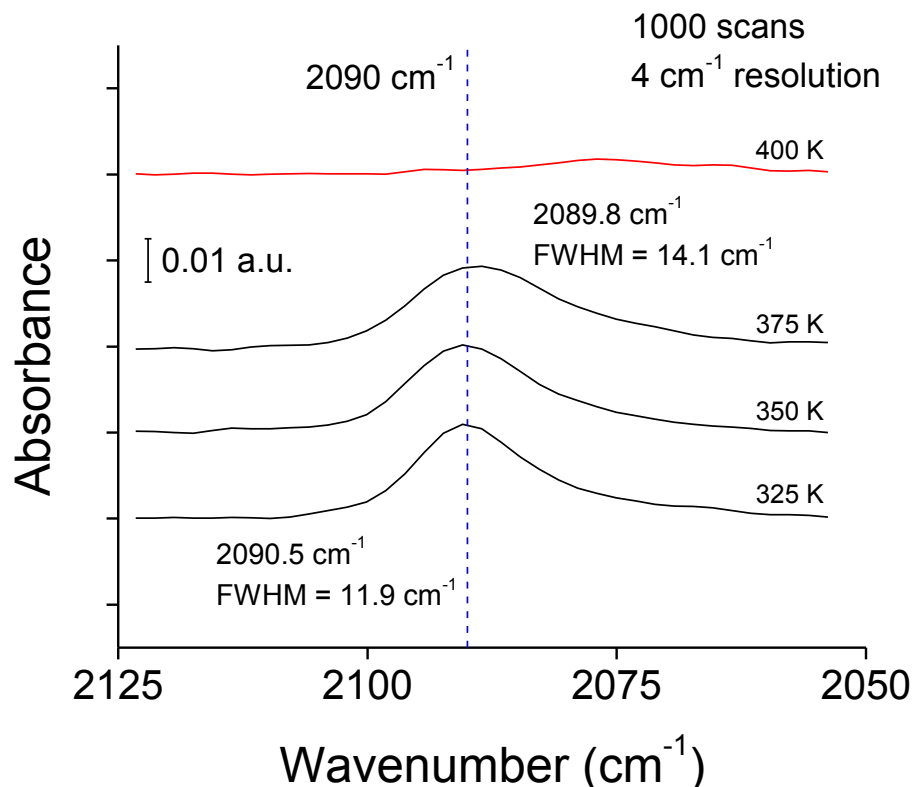
Figure 3.10. CO adsorbed on Pt(100) at 2 Torr CO, 325-400 K.

After heating the sample above 400 K, the adsorption behavior of CO on the Pt(100) surface changed. This effect is shown in Figure 3.11, which shows the same experiment conducted after heating the surface above 400 K and then cooling the sample back to 325 K, all in the presence of 2 Torr CO. An adsorption band is observed between 2077 cm^{-1} and 2079 cm^{-1} that is much broader than was observed previously. This band retains its linewidth and position as the sample is heated again from 325 K to 375 K. The band is essentially removed again at temperatures above 400 K. These results indicate that a permanent change in the surface properties can occur if the sample is heated in a CO environment.
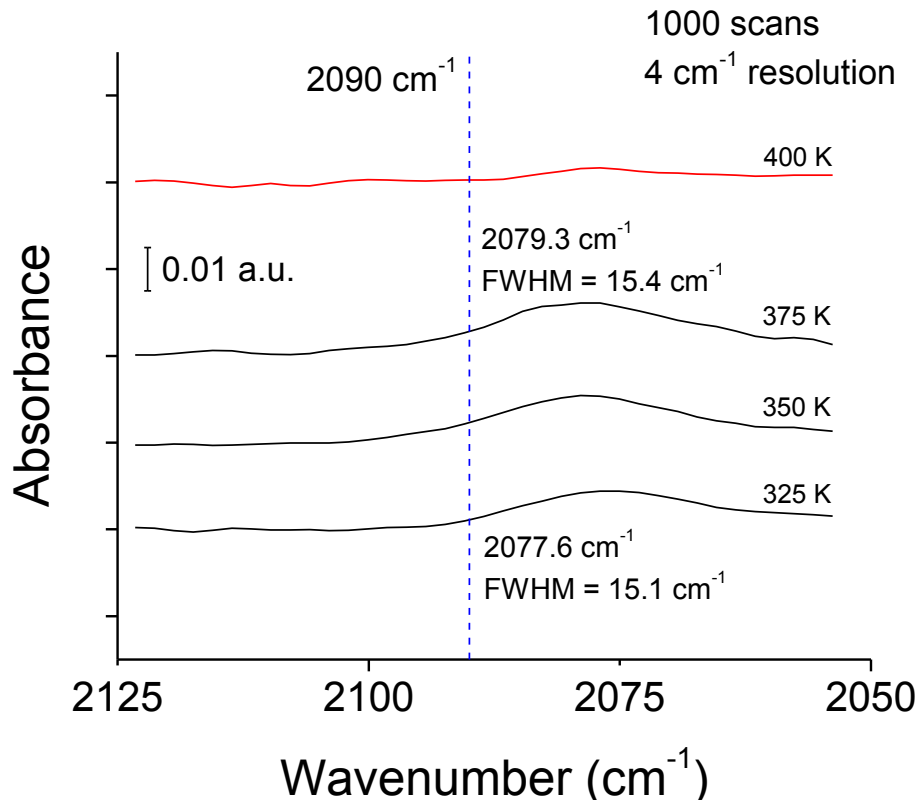
Figure 3.11. CO adsorbed on Pt(100) at 2 Torr CO after heating above 400 K.

Similar results are observed for this system under UHV conditions. PM-IRAS spectra obtained over a range of temperatures from 375 K to 575 K in the presence of 10^{-4} Torr CO are shown in Figure 3.12. The observed linear C-O absorption band exhibits significant increases in linewidth and decreases in frequency with increasing sample temperature. This observation is similar to what is observed in higher pressure conditions, as described previously. These observations are consistent with a model established by Persson which attributes these effects to a process known as phonon dephasing [8]. In this process, phonons from the bulk of the metal collide with the adsorbed CO molecules. These collisions give rise to broadening of the

observed vibrational band and a red shift in position. The symmetric broadening of the absorption band with increasing temperature observed in both Figure 3.10 and Figure 3.12 provides evidence to support the dephasing conclusion. This is because loss of phase correlation in the adsorbed molecules due to elastic collisions is known to give rise to symmetric broadening effects [9]. Phonon dephasing models have been applied to study the temperature dependence of the C-O stretch for atop CO in previous studies. For example, a continuous decrease in frequency from 2027 cm^{-1} at 90 K to 2017 cm^{-1} at 420 K with a corresponding increase in bandwidth from 4 to 7 cm^{-1} was reported for atop CO on Ru(001) [8].

As shown in Figure 3.12, the CO absorption band is essentially removed at a sample temperature of 575 K. Upon decreasing the sample temperature in the presence of 10^{-4} Torr CO, the absorption band does not return. This holds true as the sample is fully cooled to the original adsorption state of 375 K. This result indicates that sample heating is not reversible for the CO adsorption process. Instead, the surface is undergoing a permanent change to become inactive for CO adsorption.
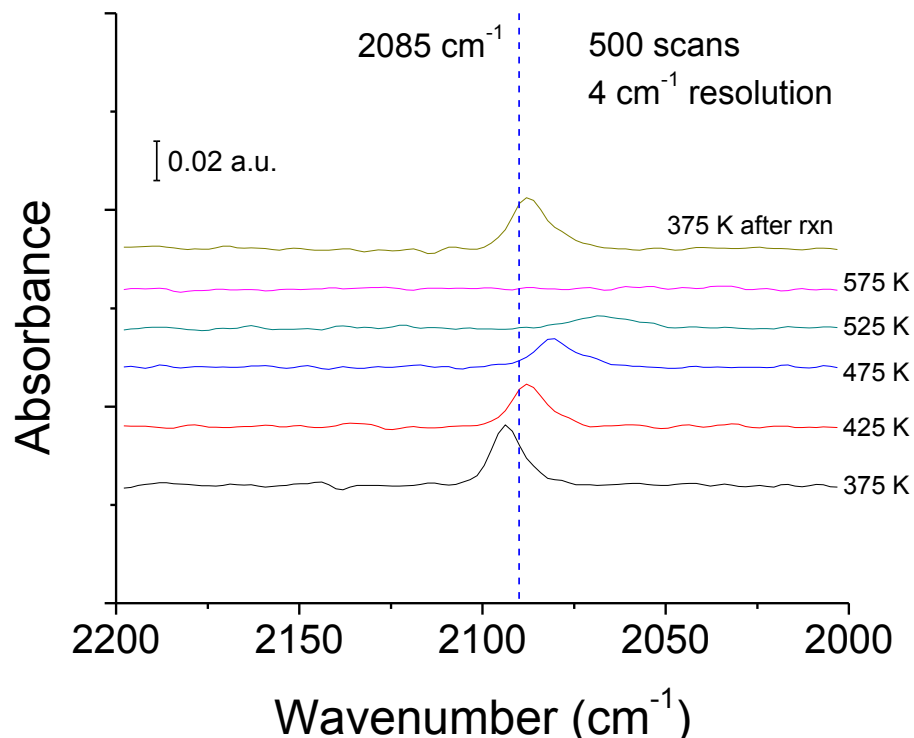
Figure 3.12. CO adsorbed on Pt(100) at 10^{-4} Torr CO, 375-575 K.

Temperature programmed desorption (TPD) experiments were conducted to investigate the possibility of desorption processes leading to disappearance of the CO absorption band. A sample TPD obtained for 100 L CO adsorbed at a temperature of 350 K is shown in Figure 3.13. The sample heating rate in this experiment was 2 K/sec. The peak desorption temperature is around 450 K. Since peak disappearance is not fully observed in Figure 3.12 until sample temperatures above 525 K are achieved, well above the observed thermal desorption state in Figure 3.13, this result excludes desorption as a likely cause of the disappearance of the CO absorption band.
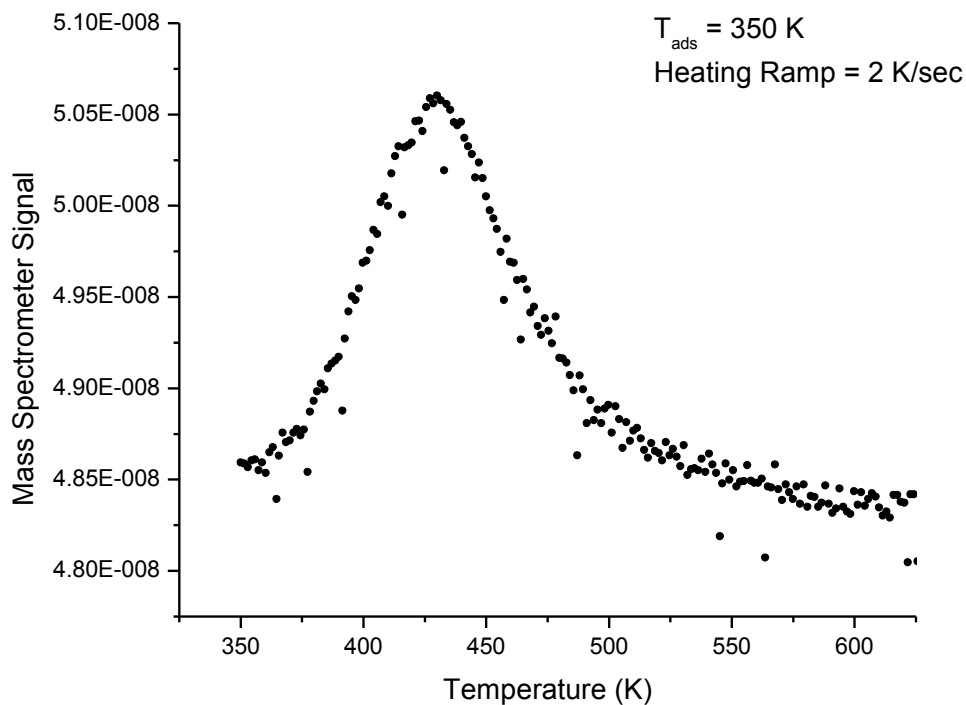
Figure 3.13. TPD of 100 L CO on Pt(100), T_{ads} = 350 K.

Exposure of the system to oxygen under CO oxidation reaction conditions, however, prompted the return of the CO absorption band. This is shown in the top spectra in Figure 3.12. For this experiment, the sample was heated to 575 K and disappearance of the absorption band was observed. Cooling of the system to 375 K resulted in no reappearance of the CO absorption band. The sample was then heated to 473 K and briefly exposed to 10^{-5} Torr O_2, all while 10^{-4} Torr CO was maintained in the reaction chamber. Upon cooling of the sample to 375 K, the CO absorption band seen in Figure 3.12 reappears. However, it doesn't exhibit the same frequency position or linewidth as the original 375 K spectra. Instead, both the frequency and

linewidth of the absorption band closely mimic that of the 425 K state. This observation could possibly be due to CO adsorption at the higher sample temperatures experienced during cooling from reaction temperatures at 473 K to the lower temperature 375 K state.

The brief introduction of oxygen into this system resulted in the re-emergence of the CO adsorption peak. This indicates that the absorption band disappearance is most likely due to carbon contamination on the surface. The contamination is lifted as the surface carbon reacts with oxygen to form CO_2. This product would then desorb from the surface, leaving behind an active surface for CO adsorption. The carbon contamination on the Pt(100) surface is attributed to CO dissociation at higher temperatures. Previous studies have determined that CO dissociation is structure-sensitive [10]. A PM-IRAS investigation excluded CO dissociation on the Pd(111) surface [11]. However, sum frequency generation experiments have identified C deposition on the Pt(111) surface due to CO dissociation during CO adsorption on Pt(111). This study determined that the resulting platinum surface was modified after CO dissociation resulted in carbon contamination on the surface [12].

The effects of sample heating on CO adsorption were also investigated at higher pressures. Integrated peak areas are calculated for CO adsorption on the Pt(100) surface in the presence of 100 Torr CO from 325 K to 550 K, as shown in Figure 3.14. The integrated peak areas are reported in terms of a relative ratio to that of the 325 K system. As the Pt(100) sample was heated in the presence of 100 Torr CO, the amount of CO adsorbed on the surface decreased steadily. At temperatures above 600 K, adsorbed CO could no longer be detected. Similarly to the UHV case,

adsorbed CO cannot be detected upon cooling of the sample after the disappearance of the absorption band. This indicates that carbon contamination inhibits CO adsorption in elevated pressure environments as well. Again, only introduction of oxygen to the system can induce CO adsorption on the surface after the system is exposed to high sample temperatures. This consistent observation of carbon contamination on the surface has important catalyst-poisoning implications for better understanding high-temperature operation of platinum catalysts in CO environments.
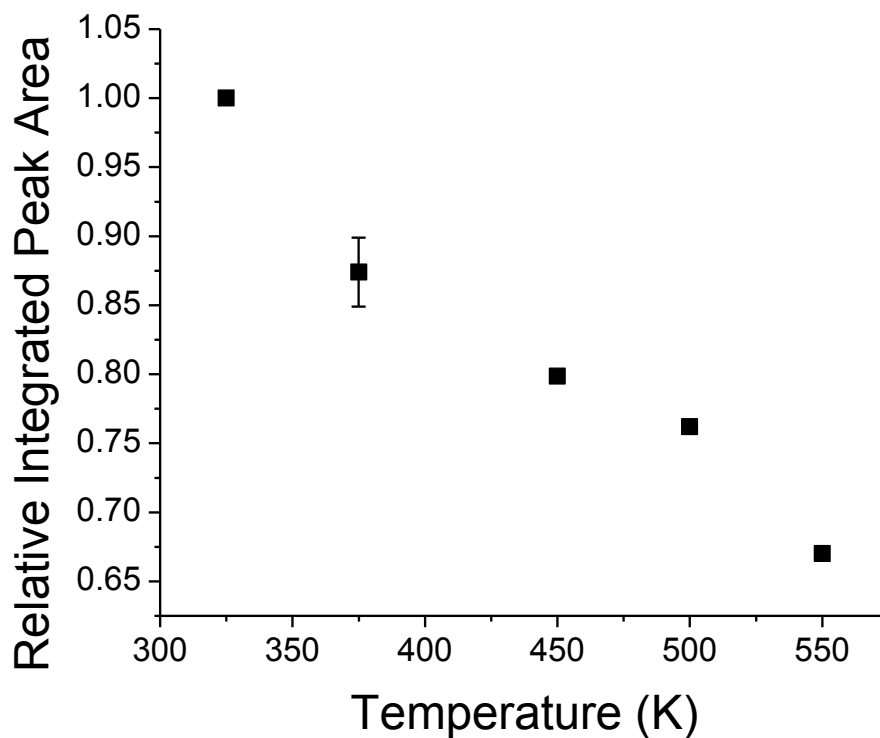

Figure 3.14. Integrated peak areas of CO adsorbed on Pt(100) at 100 Torr CO over temperature range from 325-550 K.

Based on the observation that oxygen induces the return of CO adsorption activity on the Pt(100) surface, this system was also monitored during the CO oxidation reaction to study the surface species present under reaction conditions. PM-IRAS spectra obtained for a mixture of 74% O_2/26% CO by volume at 10^{-4} Torr are shown in Figure 3.15 for sample temperatures from 373 K to 623 K. Gases were introduced to the system at a sample temperature of 373 K. The presence of CO is detected on the surface during CO oxidation at the same atop adsorption sites as in the CO adsorption experiments. As the sample is heated to 473 K, the CO peak exhibits a red shift from ~2080 cm^{-1} to ~2070 cm^{-1}, as well as a corresponding decrease in intensity. Once the sample is heated to 623 K, above the CO oxidation ignition temperature, no spectral feature is observed for these pressure conditions. This result is consistent with previous studies on platinum single crystal surfaces. Specifically, the Pt(100) surface was found to exhibit lower onset temperatures for CO dissociation and ignition of the oxidation reaction than the Pt(111) or Pt(557) surfaces [10]. It should be noted that the CO adsorption band remains present to higher temperatures than in the case of the CO-only system studied in Figure 3.12 due to the presence of oxygen in the system. This negates the effects of carbon contamination on the Pt(100) surface due to CO dissociation until CO oxidation ignition temperatures are achieved.
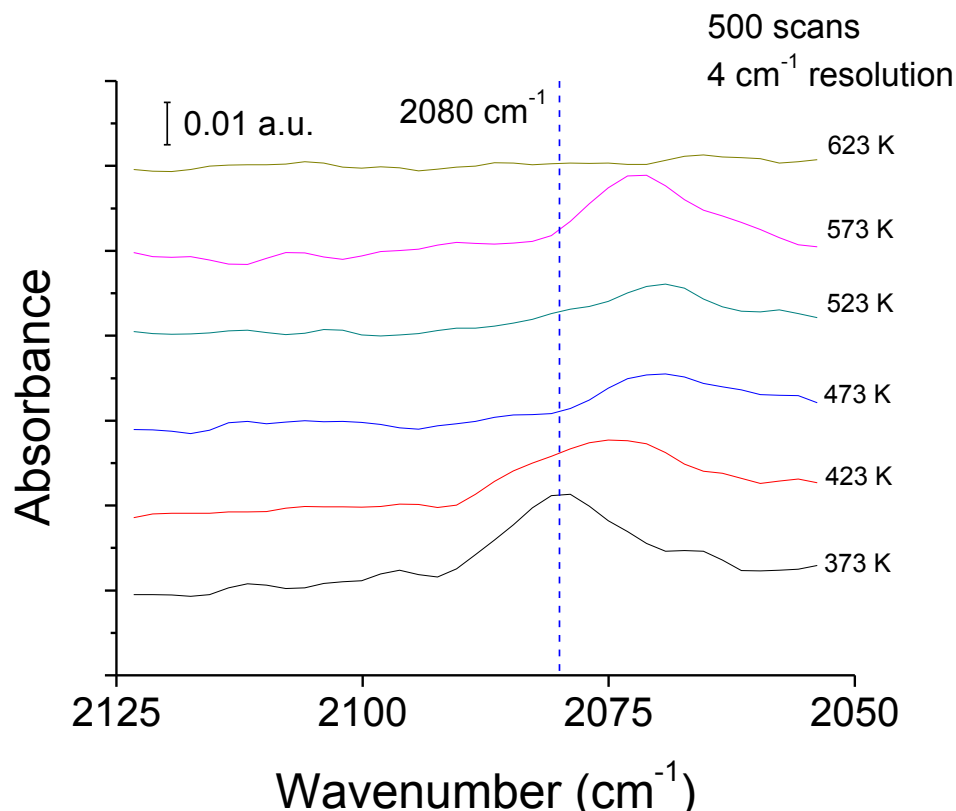
Figure 3.15. CO adsorption on Pt(100) during CO oxidation of a mixture of 74% O$_2$/26% CO by volume at 10^{-4} Torr from 373-623 K.

As an analogue to the previous adsorption experiments, recovery of the CO absorption band was tested upon cooling of the sample in the O$_2$-dominated environment. The measured spectra for this experiment are shown in Figure 3.16. Included in this figure are the spectra from Figure 3.15 prior to disappearance of the CO peak at 623 K. Cooling of the sample to 573 K does not result in the return of the CO peak. However, continued cooling to 523 K results in the return of a much sharper CO absorption band of greater intensity than is observed for the original 523 K state during heating. This result indicates that the effect of reaching ignition temperatures

for CO oxidation can lead to a more catalytically active surface for CO adsorption in an O_2-dominated environment.
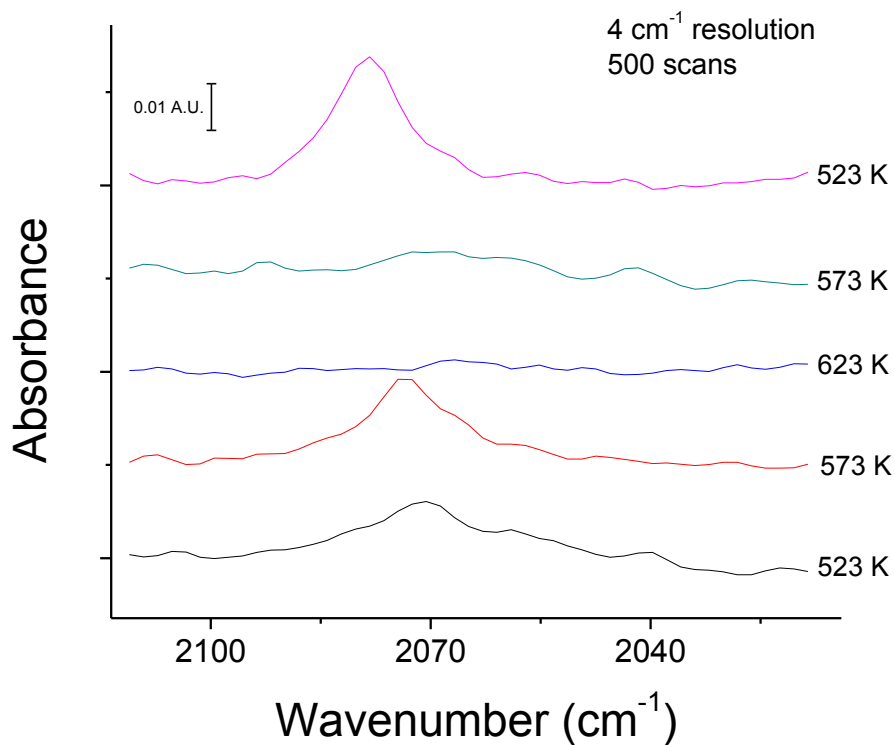
Figure 3.16. CO adsorption on Pt(100) during CO oxidation of a mixture of 74% O_2/26% CO by volume at 10^{-4} Torr during heating (below) and cooling (above) from 523-623 K.

Recovery of the CO absorption band after exposure to sample temperatures above the CO oxidation ignition temperature was also tested in a CO-dominated reaction environment. The measured PM-IRAS spectra are shown in Figure 3.17. A sharp CO absorption band exhibits decreasing frequency and intensity

during heating from 523 K to 623 K. Above 648 K, no spectral feature is observed. This indicates that the CO oxidation ignition temperature is higher in a CO-dominated environment than in an O_2-dominated environment. This is in agreement with previous studies that have determined that the ignition temperature is proportional to the CO-to-O_2 ratio [13]. Upon cooling of the sample, no CO band is observed until the emergence of a broad, weak feature at a sample temperature of 573 K. This feature does exhibit the same peak position as the original 573 K state. In contrast to the experiments in an O2-dominated environment, this result indicates that the effect of reaching ignition temperatures for CO oxidation in a CO-dominated environment leads to a less catalytically active surface for CO adsorption. In each case, however, the re-emergence of the CO peak indicates that CO adsorption and desorption are reversible processes in the presence of CO oxidation conditions. This result is in contrast to the irreversibility observed on the Pt(100) surface during CO adsorption experiments conducted in an exclusively CO environment.
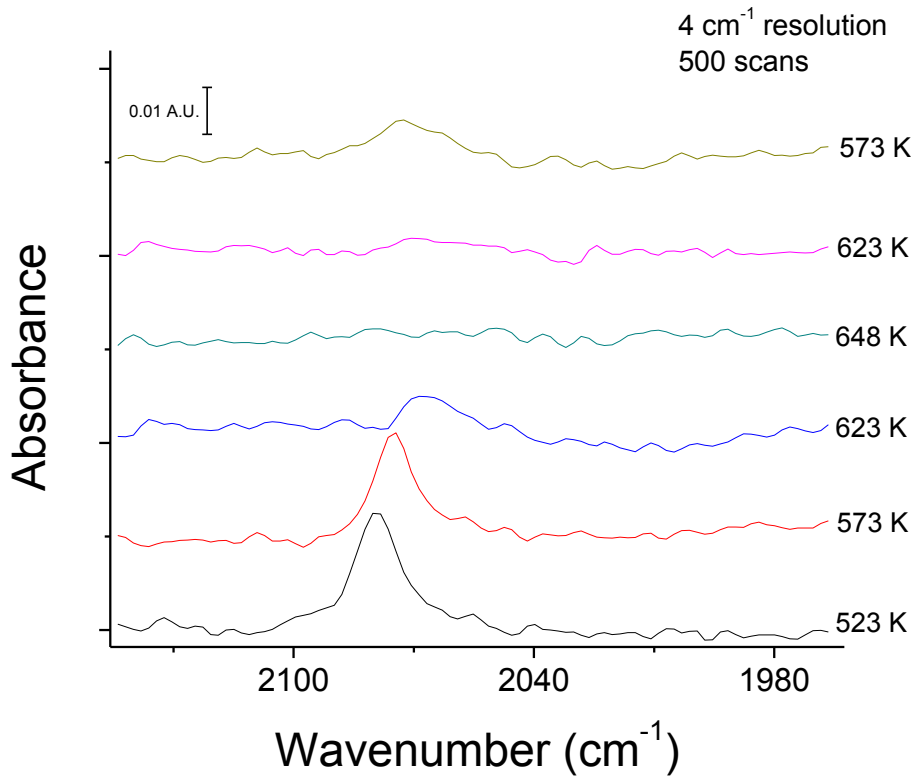
Figure 3.17. CO adsorption on Pt(100) during CO oxidation of a mixture of 26% O_2/74% CO by volume at 10^{-4} Torr during heating (below) and cooling (above) from 523-648 K.

3.3 References

[1] Yamagishi, S., Fujimoto, T., Inada, Y., Orita, H. *J. Phys. Chem. B* (2005) **109**, 8899-8908.

[2] Martin, R., Gardner, P., Bradshaw, A.M. *Surface Science* (1995) **342**, 69-84.

[3] Persson, B.N.J. *J. Electron Spectrosc. Relat. Phenom.* (1990) **54/55**, 81.

[4] Lauterbach, J., Boyle, R.W., Schick, M., Mitchell, W.J., Meng, B., Weinberg, W.H. *Surface Science* (1996) **350**, 32-44.

[5] Scheffler, M. *Surface Science* (1979) **81**, 562.

[6] Andersen, M., Johansson, M., Chorkendorff, I. *J. Phys. Chem. B* (2005) **109**, 10285-10290.

[7] Persson, B.N.J., Ryberg, R. *Phys. Rev. B* (1981) **24**, 6954.

[8] Persson, B.N.J., Hoffmann, F.M., Ryberg, R. *Phys. Rev. B* (1986) **34**, 2266.

[9] Bradshaw, A.M., Schweizer, E. "Infrared Reflection-Absorption Spectroscopy of Adsorbed Molecules." In Clark, R.J.H., Hester, R.E., editors, Spectroscopy of Surfaces, Chapter 8, Page 413. John Wiley & Sons, 1988.

[10] McCrea, K.R., Parker, J.S., Somorjai, G.A. *J. Phys. Chem. B* (2002) **106**, 10854-10863.

[11] Ozensoy, E., Min, B.K., Santra, A.K., Goodman, D.W. *J. Phys. Chem. B* (2004) **108**, 4351-4357.

[12] Kung, K.Y., Chen, P., Wei, F., Shen, Y.R., Somorjai, G.A. *Surface Science* (2000) **463**, L627-L633.

[13] Rinnemo, M., Kulginov, D., Johansson, S., Wong, K.L., Zhdanov, V.P., Kasemo, B. *Surface Science* (1997) **376**, 297.

Chapter 4

REVERSE MICELLE SYNTHESIS OF RUTHENIUM NANOPARTICLES

4.1   Introduction

Chapter 3 described high pressure experiments designed to bridge the "pressure gap" to facilitate comparisons between surface science investigations and industrial catalytic performance near atmospheric pressures and above. Similarly, methods are required to bridge the "materials gap" between model catalysts consisting of single crystal surfaces and supported nanoparticles which more closely mimic industrial catalysts. This objective is accomplished through investigation of the reverse micelle technique for nanoparticle catalyst synthesis. In particular, the ability to synthesize nanoparticle catalysts of specific sizes with low dispersion is an important objective in this work. Preliminary experiments have focused on developing a synthesis procedure for nanoparticle catalysts. The development of the reverse micelle technique for catalyst synthesis is a parallel track to the high-pressure PM-IRAS experiments described previously. Ultimately, combination of nanoparticle synthesis techniques with ambient pressure investigations would allow for bridging both the pressure and materials gaps between model surface science studies and industrial catalytic performance.

4.2   Experimental

4.2.1   Reverse Micelle Technique

Reverse micelle microemulsions were formed through the mixing of an oil solution, water, and a surfactant with both hydrophobic and hydrophilic components. Several microemulsion system chemistries were studied in this work. Each of these systems contained an oil solution, surfactant system with optional co-surfactant, and water. Surfactants that were investigated included Brij-30 ($(C_{20}H_{42}O_5)_n$), isooctyl phenoxy polyethoxy ethanol (Triton X-100, $4\text{-}(C_8H_{17})C_6H_4(OCH_2CH_2)_nOH$, n~10), and butyl ammonium laurate ($[CH_3CH_2CH_2CH_2NH_3^+]$ $[C_{11}H_{23}COO^-]$). In the case of the Brij-30 and Triton X-100 systems, cyclohexane was used as the oil phase. Hexanes was used as the oil phase in the butyl ammonium laurate system.

Reverse micelle microemulsions were prepared over a range of ω values, where ω is defined as the molar ratio of water to surfactant in the microemulsion system. Syntheses were performed under ambient bench-top conditions. For the water-butyl ammonium laurate-hexanes microemulsion system, each microemulsion sample was prepared by adding lauric acid and butyl amine in equimolar quantities to hexanes. 99.8% butyl amine, 99.5+% lauric acid, and 99.8% hexanes were purchased from Aldrich and used without further purification. The water-to-surfactant ratio of the final microemulsion solution was then adjusted by the addition of an appropriate amount of deionized water. Reaction of the butyl amine and lauric acid components in the presence of water yielded butyl ammonium laurate surfactant molecules. This process of reverse micelle formation is shown in Figure 4.1 [1]. The butyl ammonium laurate surfactant was chosen due to its ease of removal from the final particle surface based on calcination temperature requirements as low as 200^oC [2].

62
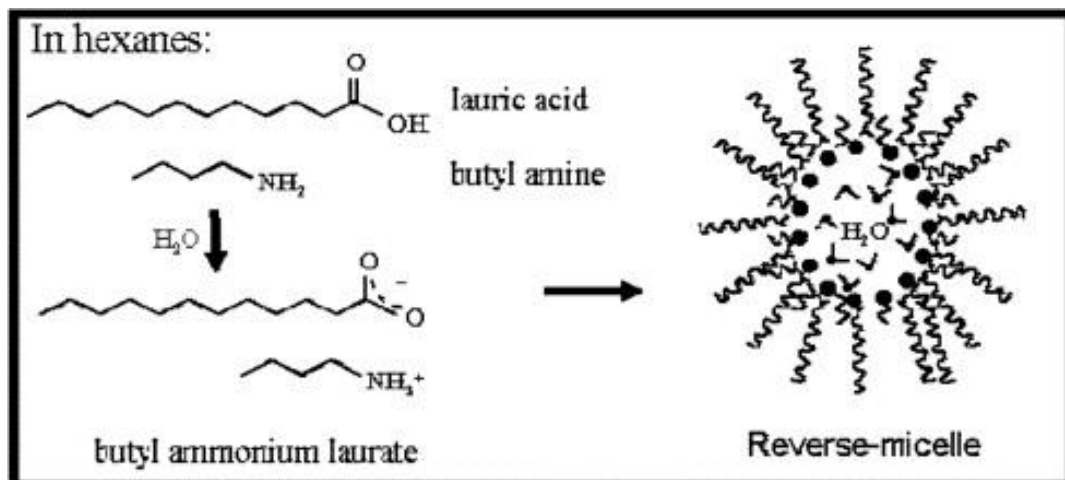
Figure 4.1.   Synthesis of butyl ammonium laurate reverse micelles [1].

Ruthenium nanoparticles were synthesized using reverse micelle microemulsions prepared as described previously based upon the selection of an appropriate water-to-surfactant ratio for desired nanoparticle size. For the synthesis procedure, two separate and identical reverse micelle microemulsions were used. $RuCl_3$ was used as the catalyst precursor and was added to one of the prepared microemulsions. An appropriate quantity of $RuCl_3$ was selected so that the ruthenium ions concentrated in the aqueous phase inside the reverse micelles at a concentration of 0.1 M. Sodium borohydride, $NaBH_4$, acting as the reducing agent, was then added to the other identically-prepared microemulsion. These reducing agent ions also concentrated within the aqueous phase of the second microemulsion. The amount of $NaBH_4$ added was in excess of fifteen times the ruthenium ion concentration in order to ensure the complete reduction of the ruthenium ions. The two microemulsions were then combined to stimulate synthesis of ruthenium particles. Intermixing of the two solutions led to coalescence of reverse micelles containing each reactant. This process

is shown in Figure 4.2 [3]. In this process, reverse micelles containing metal ions and reverse micelles containing reducing agent interacted through the process of micellar diffusion. When two reverse micelles came into contact, they coalesced and the surfactant layer opened between the two, essentially forming a single larger micelle. The contents were then free to intermix via molecular diffusion within the single reverse micelle, stimulating nucleation of Ru nanoparticles. These larger reverse micelles then typically decoalesced into two separate reverse micelles, each containing a seeded Ru nanoparticle.
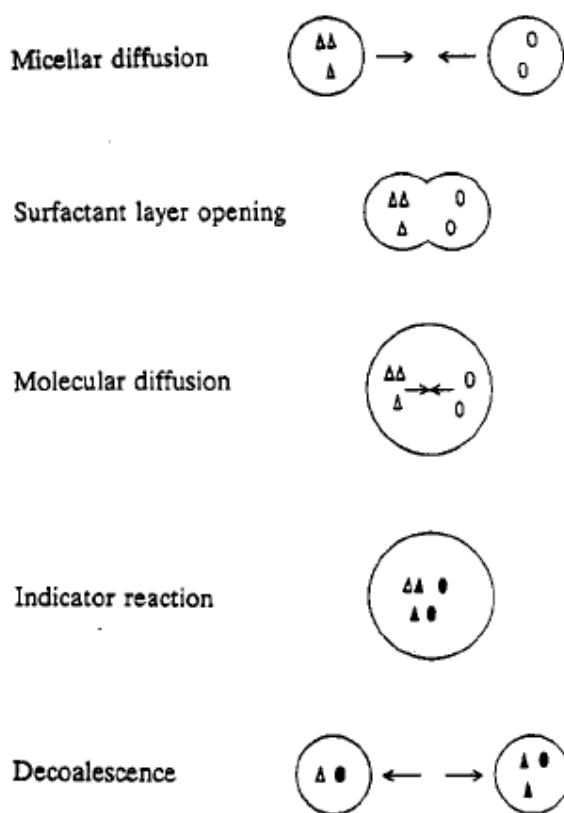

Figure 4.2.   Reverse micelle reaction mixing process [3].

4.2.2   Characterization Techniques

Prepared microemulsions were characterized using Dynamic Light Scattering (DLS) to determine the size of the synthesized reverse micelles. Light scattering data were collected using a BI-9000AT digital autocorrelator, BI-200SM goniometer, and 9KDLSW control program (Brookhaven Instruments). To obtain dust-free samples, the microemulsions were filtered using a 450 nm PTFE mesh, and the contents were injected into a clean glass cuvette. The incident light source was provided by a model 95 argon ion laser (Lexel Laser) operating at a wavelength of 488 nm. Data were collected at a scattering angle of 90°. The diffusion coefficient for the reverse micelles was calculated by solution of the autocorrelation function under the assumptions that the particles were spherical and the solution viscosity was that of hexanes in the case of the butyl ammonium laurate microemulsions and cyclohexane in the cases of Brij-30 and Triton X-100 microemulsions. Solution of the Stokes-Einstein equation, shown in Equation 4.1, allowed for determination of the hydrodynamic radii of the reverse micelles [4].

$$D = \frac{k_B T}{6\pi\eta R_H} \tag{4.1}$$

In this equation, η is the viscosity of the fluid, k_B is the Boltzmann constant, T is the absolute temperature of the dispersion, and R_H represents the hydrodynamic radius.

Small-Angle X-ray Scattering (SAXS) was used to characterize particle size in reverse micelle microemulsions prepared using the butyl ammonium laurate reverse micelle microemulsion system chemistry. In this experiment, microemulsions containing only reverse micelles and microemulsions containing the synthesized

ruthenium particles were analyzed and compared. SAXS patterns were collected on a SAXSess instrument (Anton-Paar) using line collimated Cu Kα radiation (1.542 Å) and a phosphor image plate. The sample holder is a TCS120 (Anton-Paar) that is fitted for liquid samples in a quartz capillary (1 mm diameter). A hexanes background was subtracted from each experimental scattering pattern.

4.3 Results and Discussion

DLS experiments indicate the formation of reverse micelles in a hexanes-water-butyl ammonium laurate microemulsion. Analysis of the autocorrelation function indicates that reverse micelles were synthesized in the range of 5-30 nm. Variation in the size of the reverse micelles over a range of water-to-surfactant ratios is shown in Figure 4.3. Experimental data are shown in comparison to results obtained by Hoefelmeyer, et al [1]. The error bars shown for the experimental data take into account the repeatability from day-to-day variations. Unfortunately, no error bars are reported for the Hoefelmeyer results. The experimental data show good consistency with the results from Hoefelmeyer at a water-to-surfactant ratio of four. However, discrepancies develop between the experimental data and Hoefelmeyer results at higher water-to-surfactant ratios. This could be due in part to changes in viscosity within the microemulsion as the water content is increased. For these data, the solvent viscosity is taken to be equivalent to that of hexanes.   A study testing variability in reverse micelle sizes from prepared microemulsions is conducted for a series of microemulsions. This is shown in Figure 4.4 for microemulsion systems with water-to-surfactant ratios equal to 6. This study indicates that reverse micelles at lower ω values can be consistently synthesized within a range of a few nanometers.
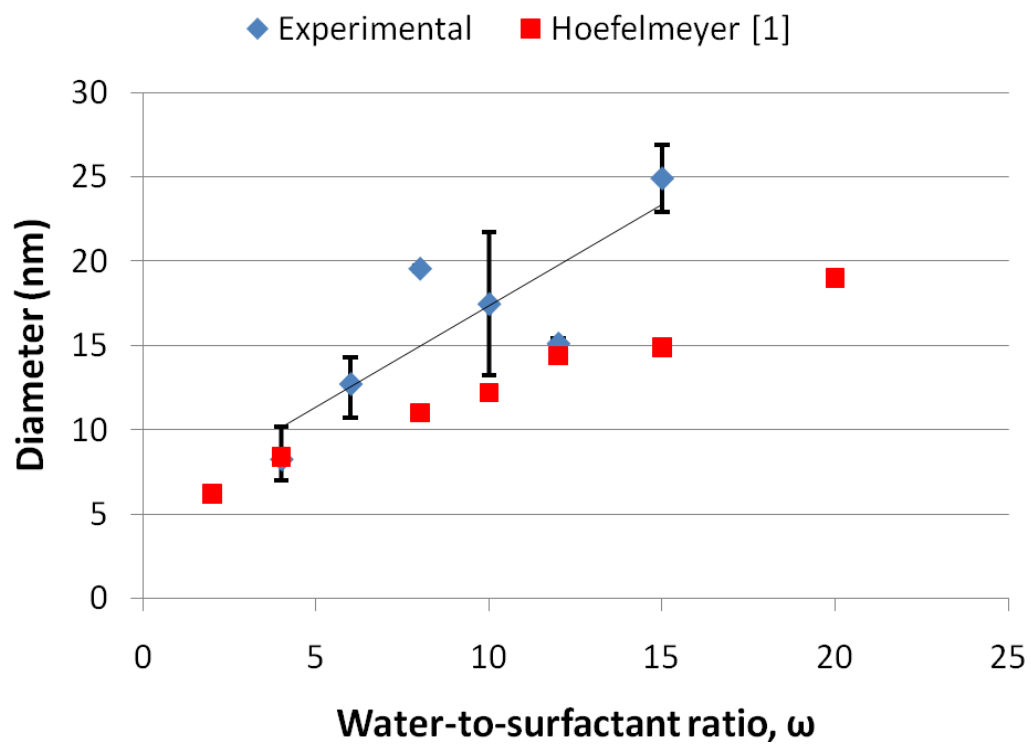
Figure 4.3. Variation in reverse micelle diameter over a range of water-to-surfactant molar ratios in hexanes-water-butyl ammonium laurate microemulsions characterized with DLS.
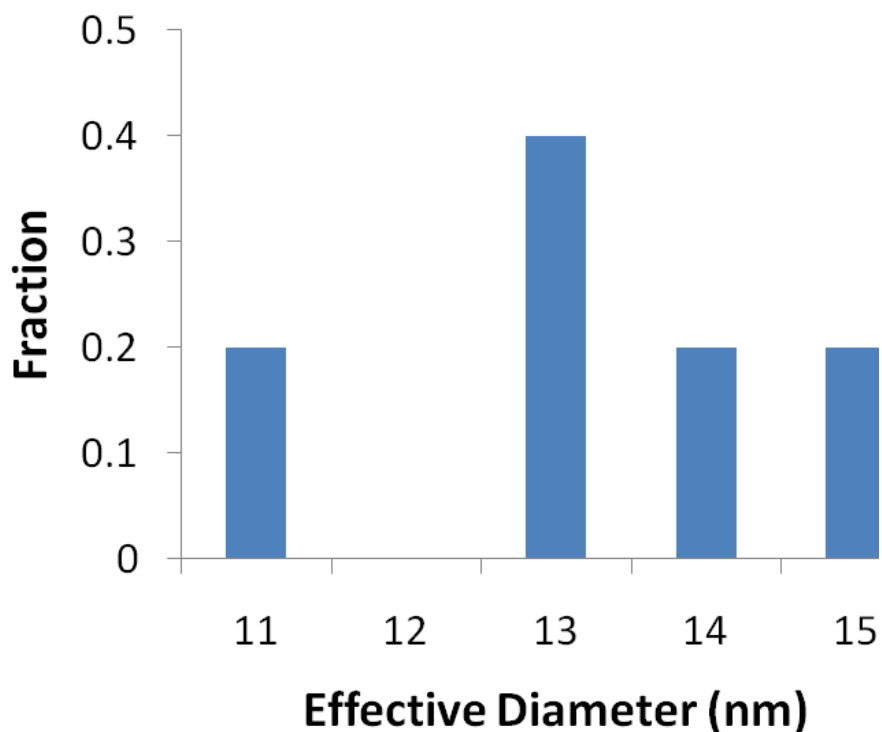
Figure 4.4. **Reverse micelle diameter variabilty study of reverse micelle synthesis procedure (ω = 6).**

Microemulsions with a water-to-surfactant ratio of four were selected for synthesizing small ruthenium particles (<5 nm). This selection was based on a comparison between the previous results and the observation from previous studies that show that final particle size is typically two to three times smaller than reverse micelle size [1]. SAXS experiments were conducted for a microemulsion containing only "empty" reverse micelles (ω = 4), as well as for an equivalent microemulsion containing synthesized ruthenium particles. The scattering results are shown in Figure 4.5 in reciprocal space with the corresponding particle size analysis shown in a distance distribution function in Figure 4.6. The scattering results indicate that reverse

micelles were synthesized with an average radius of 3-4 nm. It is expected that very little scattering is seen from the surfactant tail due to the fact that its composition is very similar to that of hexanes. As a result, only one scattering length was observed. The synthesized ruthenium particles were found to have an average diameter of ~3 nm, measuring ~50% smaller than the reverse micelles in which they were contained. This result is in agreement with previous studies [1]. As expected, the scattering data for the microemulsion containing synthesized Ru particles register intensity above the scattering data for the microemulsion containing "empty" reverse micelles for greater lengths of the scattering vector ($q > 1.5$ nm^{-1}). However, the recorded intensity for the nanoparticle-containing microemulsion is less than that of the control microemulsion below this threshold. A possible explanation for this observation is that the scattering length scale of the ruthenium particle and the space between the surfactant head groups and the ruthenium particle are very similar. This is a reasonable explanation based on the mean lengths determined for the distance distribution functions of the compared microemulsions.
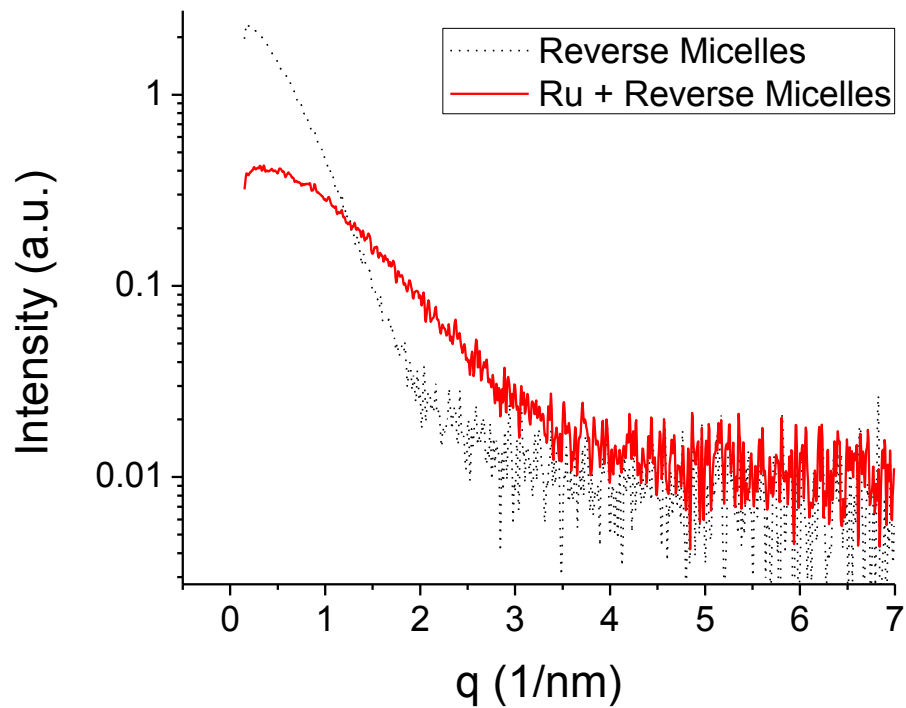
Figure 4.5. SAXS results for synthesized hexanes-water-butyl ammonium laurate reverse micelles and hexanes-water-butyl ammonium laurate reverse micelles containing synthesized Ru particles ($\omega = 4$).
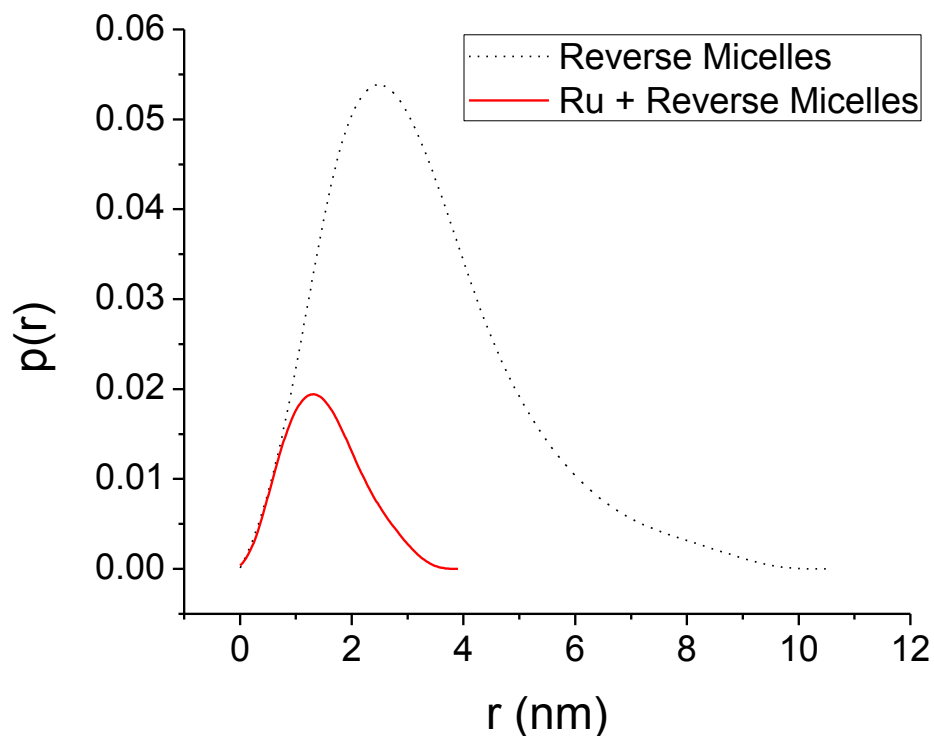
Figure 4.6. **Distance distribution functions from SAXS results for synthesized hexanes-water-butyl ammonium laurate reverse micelles and reverse micelles containing synthesized Ru particles ($\omega = 4$).**

Verification of the previous results could proceed through the use of Cryogenic Transmission Electron Microscopy to complete a detailed comparison of the properties of reverse micelle microemulsions as compared to microemulsions containing synthesized nanoparticles. These studies could corroborate the conclusions drawn from the SAXS experiments.

Further development of the reverse micelle synthesis method for producing nanoparticles of specific sizes is possible through the inclusion of additional parameters in the synthesis process to provide further tunability for the technique.

Previous studies have shown that particle size is dependent on the temperatures employed during the synthesis process [5]. A better understanding of the effect of temperature on the reverse micelle synthesis process would provide another parameter in order to further tune the system for synthesizing desired nanoparticles.

Thus far, the reverse micelle synthesis method has been performed in parallel to the PM-IRAS high pressure investigations. The potential exists to bridge the two methods to allow for characterization of synthesized nanoparticle catalysts using high-pressure spectroscopic techniques. One possibility for linking these parallel paths is through the growth of atomically flat, crystalline thin oxide films as catalyst supports. A thin oxide support, such as Al_2O_3, does not interfere with infrared measurements, providing an excellent platform for fundamental catalytic studies [6]. These oxide supports can be grown in situ, in the reaction chamber under ultra-high vacuum conditions. The work of Wallace, et al., has shown that films of a uniform thickness can be prepared using this method [7]. Preparation of the samples in situ prevents degradation and allows for a controlled environment in which to set up the reaction experiments.

The work to date has shown that the reverse micelle method is a promising technique for synthesizing nanoparticle catalysts. Supporting these nanoparticles on thin oxide supports for spectroscopic investigation provides a means to bridge the materials gap commonly found in surface science studies. Combining these capabilities with PM-IRAS analysis will allow for fundamental studies over a wide range of reaction conditions from UHV to ambient pressures, facilitating comparisons with the performance of industrial catalysts.

4.4 References

[1] Hoefelmeyer, J.D., Liu, H., Somorjai, G.A., Tilley, T.D. *Journal of Colloid and Interface Science* (2007) **309**, 86-93.

[2] Pérez-Dieste, V., Castellini, O.M., Crain, J.N., Eriksson, M.A., Kirakosian, A., Lin, J.-L., McChesney, J.L., Himpsel, F.J. *Applied Physics Letters* (2003) **83**, 5053.

[3] Bommarius, A.S., Holzwarth, J.F., Wang, D.I.C., Hatton, T.A. *J. Phys. Chem.* (1990) **94**, 7232-7239.

[4] Hiemenz, P.C., Rajagopalan, R. Principles of Colloid and Surface Chemistry: 3rd Edition. Marcel Dekker, Inc.: New York, 1997.

[5] Lin, X.M., Sorensen, C.M. *Langmuir* (1998) **14**, 7140-7146.

[6] Rupprechter, G. *Catalysis Today* (2007) **126**, 3-17.

[7] Wallace, W.T., Min, B.K., Goodman, D.W. *Topics in Catalysis* (2005) **34**, 17-30.

Chapter 5

CONCLUSIONS

Polarization modulation infrared reflection absorption spectroscopy (PM-IRAS) is an experimental technique that has been applied to a number of catalytic chemistries. It allows for molecular-level catalytic investigations in the presence of near-ambient pressures closer to industrially-relevant conditions. In this work, the PM-IRAS technique is shown to be highly effective for detecting adsorbed surface species on metal single crystal samples in the presence of near-atmospheric pressure conditions.

The PM-IRAS system is capable of monitoring model catalytic systems under reaction conditions. Carbon monoxide adsorption and oxidation behavior are investigated on a Pt(100) single crystal surface. The PM-IRAS system is able to detect adsorbed CO on Pt(100) in the presence of up to ~200 Torr CO. At a sample adsorption temperature of 325 K, atop sites are occupied on Pt(100) by CO for pressures between 1 and 200 Torr CO. An additional frequency shift of up to 6 cm^{-1} is observed from 1 to 200 Torr CO due to dipole-dipole coupling. No new high-pressure adsorption sites are observed. However, CO coverages much higher than any observed under UHV conditions are found to be present at these high pressure conditions.

A dipole-coupling model was applied to these experimental results. The model predicted CO surface coverages on the Pt(100) surface increasing from ~0.7 at 1 Torr CO to ~0.95 at 200 Torr CO. These results indicate that at higher pressures the

CO surface coverage on Pt(100) is much greater than similar measurements obtained under UHV conditions. The predicted increases in surface coverage at higher pressures were verified through analysis of the integrated peak areas of the measured absorption bands. The calculated areas were observed to increase by up to 50% in magnitude over the pressure range from 1 Torr CO to 200 Torr CO.

These higher coverages achieved at high pressure conditions are not found to be fully stable upon reduction of system pressure. This indicates that the high-pressure CO adsorption behavior is a mixture of both reversible and irreversible processes. This is in contrast to observations at lower pressures and provides insight into variation in system behavior under near-ambient pressure conditions.

In contrast, heating of the sample at any pressure led to irreversible changes in surface adsorption behavior. Sample heating caused the atop site band to broaden and shift to lower frequencies due to phonon dephasing effects. Above certain sample temperatures, the absorption band associated with adsorbed CO is no longer observed in the measured spectra. This effect is attributed to CO dissociation at higher sample temperatures, resulting in carbon contamination on the Pt(100) surface. Carbon contamination on the surface ultimately deactivated the catalyst until oxygen was added to the system to regenerate surface adsorption behavior. Subsequent spectra obtained after exposure of the system to oxidative conditions reveal the return of the absorption band corresponding to adsorbed CO. Temperature programmed desorption (TPD) measurements also corroborate this finding by excluding desorption as a likely cause of the loss of the CO band. These findings lend insight into potential poisoning effects of platinum catalysts operating at high temperatures in CO environments.

In parallel to the spectroscopic investigations, preliminary work is presented for bridging the materials gap through investigation of the reverse micelle nanoparticle synthesis technique. Of the three microemulsion systems investigated in this work, only solutions containing butyl ammonium laurate surfactant are shown to provide for reproducible synthesis of reverse micelles. The reverse micelle synthesis process is shown to be tunable and exhibits small variation in reverse micelle size at low water-to-surfactant ratios. Ruthenium nanoparticles are successfully synthesized using the reverse micelle technique and measured to be over a factor of 2 smaller in diameter than the reverse micelles in which they are synthesized.

Through investigation of model catalytic systems at near-ambient pressure conditions using the PM-IRAS technique, this work bridges the pressure gap to study surface adsorption behavior at pressures near industrial operating conditions. In parallel, the synthesis of catalyst nanoparticles with controlled particle size using the reverse micelle technique bridges the materials gap to allow examination of structure effects. The combination of these two parallel tracks provides a path to investigate systems closely mimicking those of industrial catalysts through the study of supported nanoparticle catalysts over a wide range of reaction conditions from UHV to ambient pressures.